Supplementary Information

The role of exciton lifetime for charge generation in organic solar cells at negligible energy level offsets

Andrej Classen,[1] Christos L. Chochos,[2,3] Larry Lüer,*[1] Vasilis G. Gregoriou,[2,4] Jonas Wortmann,[1] Andres Osvet,[1] Karen Forberich,[1] Iain McCulloch,[5,6] Thomas Heumueller,*[1] and Christoph J. Brabec*[1,7,8]

[1] *Institute of Materials for Electronics and Energy Technology (i-MEET), Friedrich-Alexander University Erlangen-Nürnberg, Martensstraße 7, 91058 Erlangen, Germany.*

[2] *Advent Technologies SA, Stadiou Street, Platani, Rio, Patras 26504, Greece.*

[3] *Institute of Chemical Biology, National Hellenic Research Foundation (NHRF), 48 Vassileos Constantinou Avenue, 11635 Athens, Greece.*

[4] *National Hellenic Research Foundation (NHRF), 48 Vassileos Constantinou Avenue, 11635 Athens, Greece.*

[5] *Department of Chemistry and Centre for Plastic Electronics, Imperial College London, London SW7 2AZ, UK.*

[6] *King Abdullah University of Science and Technology (KAUST), KAUST Solar Center (KSC), Thuwal 23955-6900, Saudi Arabia.*

[7] *Helmholtz-Institute Erlangen-Nürnberg (HI ERN), Immerwahrstraße 2, 91058 Erlangen, Germany.*

[8] *Bavarian Center for Applied Energy Research (ZAE Bayern), Immerwahrstraße 2, 91058 Erlangen, Germany.*

E-mail: thomas.heumueller@fau.de, larry.lueer@fau.de, christoph.brabec@fau.de

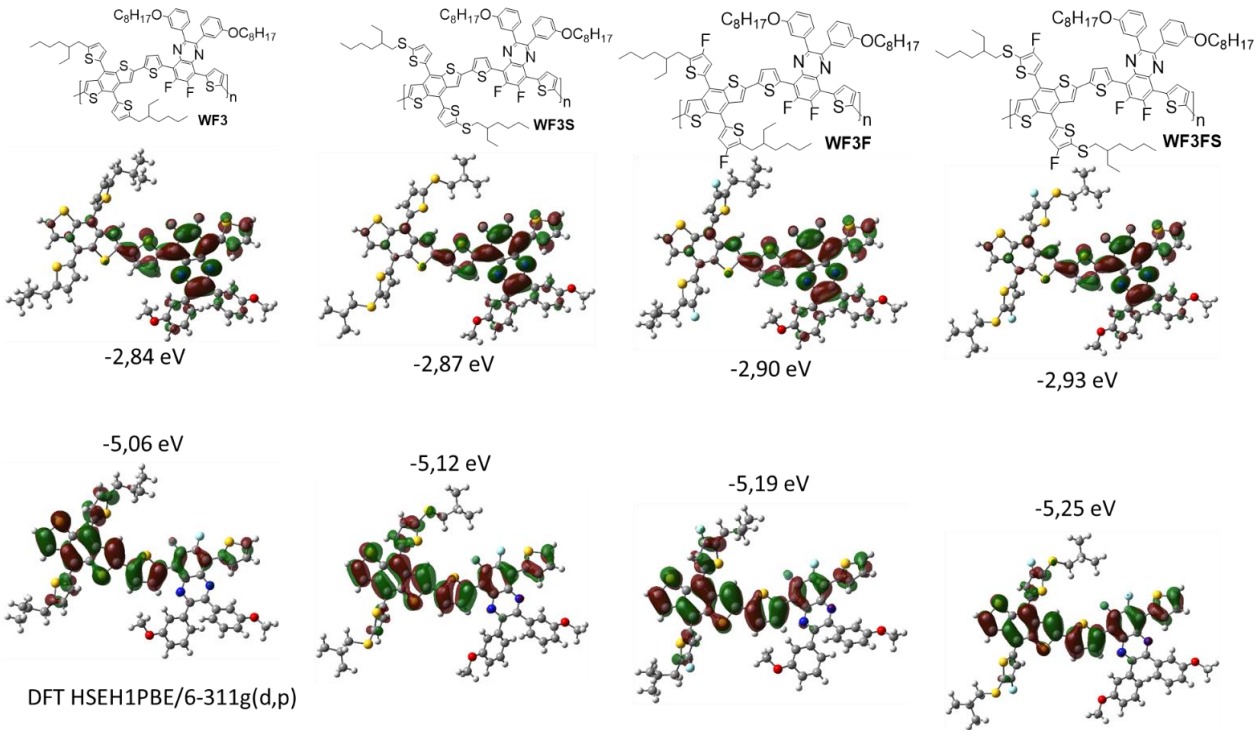

Supplementary Figure 1 | Calculated energy levels based on density functional theory. The combined sulfonation and fluorination strategy allows for a fine tuning of the HOMO levels in WF3, WF3S, WF3F and WF3FS. For details of the calculation see Methods section in the main text.

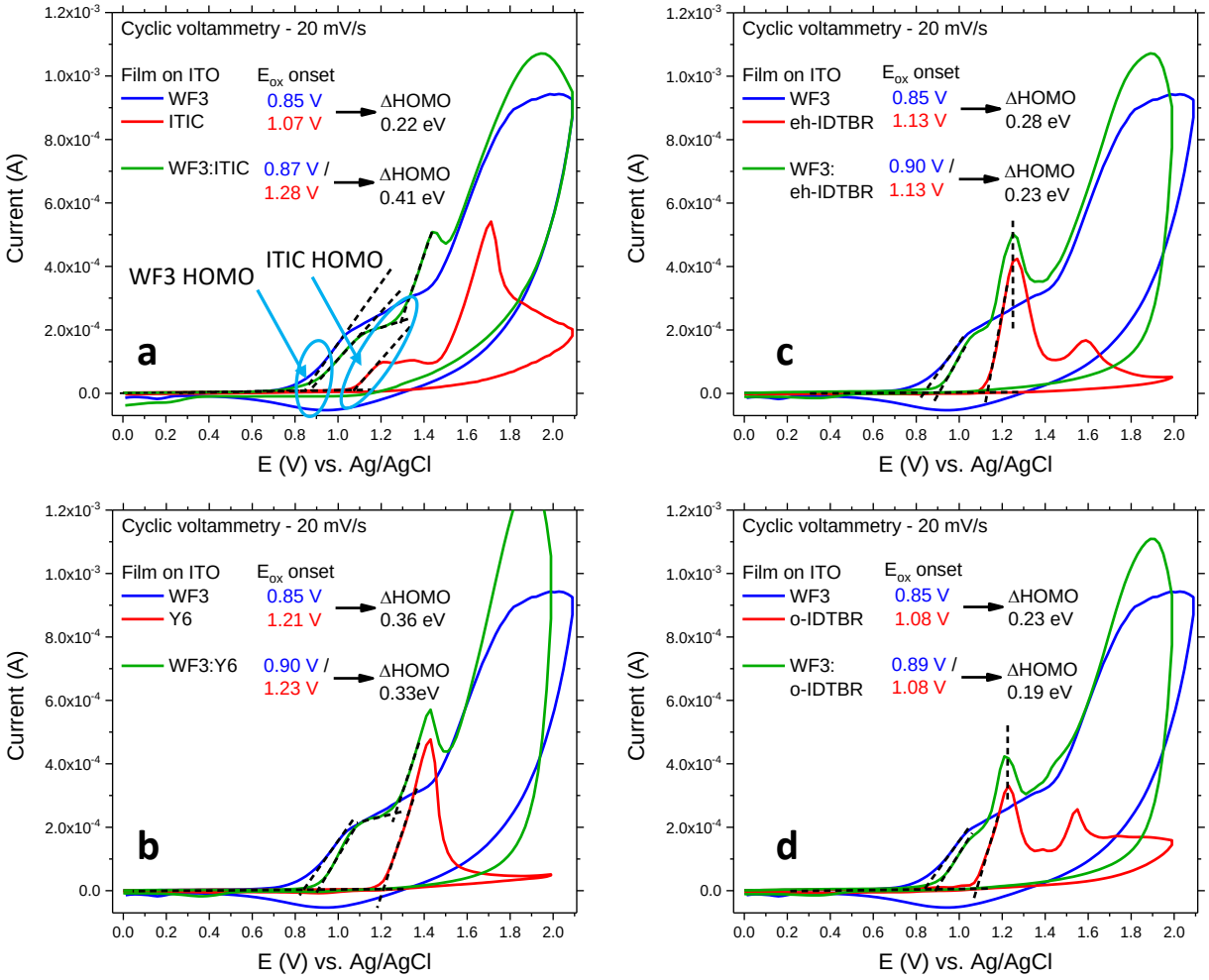

Supplementary Figure 2 | Cyclic voltammetry measurements of pristine material and BHJ films. The onset of oxidation reveals E_{HOMO} with respect to the reference Ag/AgCl electrode, which is determined via the intersection of the linear fit (dashed lines) in the regime before the onset of oxidation and of the linear fit (dashed lines) in the oxidation regime. The blue arrows in **a)** highlight this intersection point.**a)** CV ofWF3, ITIC and WF3:ITIC. **b)-d)** CV of WF3, Y6, eh-IDTBR, o-IDTBR, WF3:Y6, WF3:eh-IDTBR and WF3:o-IDTBR. A difference of 0.22 eV in E_{HOMO} between pristine WF3 and ITIC is detected. However, in a BHJ E_{HOMO} of ITIC changes significantly which results in a difference of 0.41 eV for E_{HOMO} between WF3 and ITIC.For the other NFAs the HOMO levels do not change significantly.

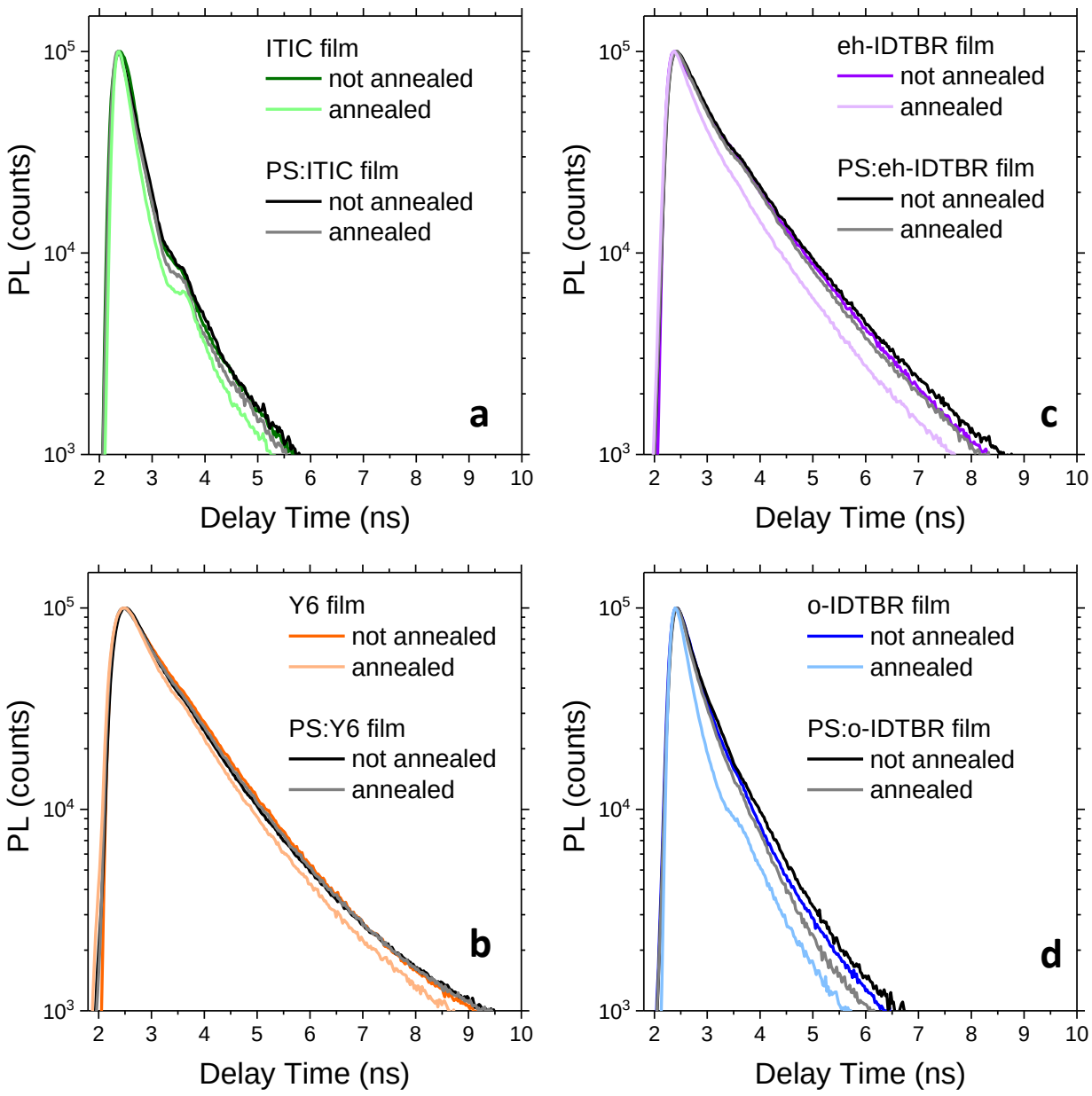

Supplementary Figure 3 | TRPL measurements to investigate the impact of microstructure. TRPL measurement of layer on glass of **a)** annealed and non-annealed ITIC and annealed and non-annealed polystyrene:ITIC. **b)** annealed and non-annealed Y6 and annealed and non-annealed polystyrene:Y6. **c)** annealed and non-annealed eh-IDTBR and annealed and non-annealed polystyrene:eh-IDTBR. **d)** annealed and non-annealed o-IDTBR and annealed and non-annealed polystyrene:o-IDTBR. The polystyrene:acceptor films are measured in order to replicate the condition in a BHJ organic solar cell. However, the TRPL decay curves for non-annealed pristine acceptor films and for both polysterne:acceptors films are almost identical. Only for a annealed pristine acceptor film a clearly faster PL decay is observed. This demonstrates that the exciton decay in non-annealed acceptor films is representative for BHJ organic solar cells.

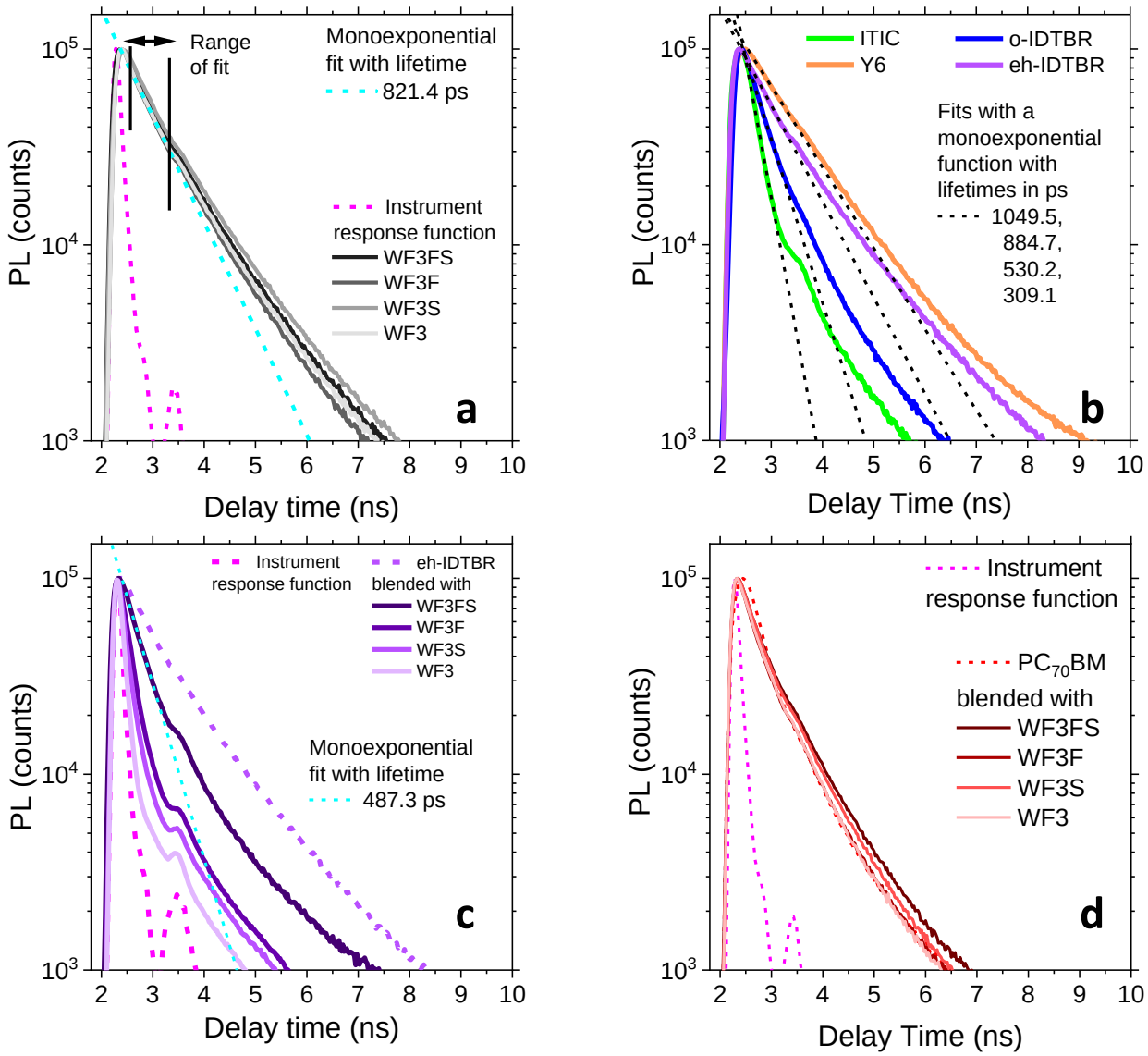

Supplementary Figure 4 | TRPL measurements and fits of TRPL measurements. On the logarithmic scale an exponential PL decay and an exponential fit function appear as linear lines. In a short range of several TRPL decay curves an exponential decay is observed and thus fitted with an exponential function, see Supplementary Note 1 for details. **a)** TRPL measurements of all polymers used in this work (same data as shown in Figure 2a in the main text) and a mono-exponential fit of the WF3 signal which yields an exciton lifetime of 821 ps. **b)** Fit of the TRPL signals of pristine ITIC, Y6, eh-IDTBR and o-IDTBR with mono-exponential functions. **c)** Fit of WF3FS:eh-IDTBR with a mono-exponential function. **d)** Time-resolved PL measurements of all $PC_{70}BM$ solar cells. The signal of all blends resembles the signal of pristine $PC_{70}BM$ and thus does not capture the quenching of excitons by the donor:acceptor heterojunction, as is observed for all other composites (see main text Figure 2). Due to the large energy offsets at the donor:acceptor interface (see Figure 1b main text) we expect a time regime on the order of 100 fs for the charge transfer and quenching of excitons. Hence we reason that our experimental setup is not able to capture the ultra-fast quenching of excitons at the donor:acceptor interface and what we measure instead are just some non-split excitons which decay in some isolated $PC_{70}BM$ domains.

Supplementary Note 1: Fitting and analysis of TRPL data

To extract decay lifetimes from experimental data, it is necessary to fit the measured TRPL data. By doing this, it is possible to determine the characteristic exciton lifetimes in pristine material films or to determine the PL quenching lifetime in BHJ organic solar cells. By considering that PL quenching in a BHJ is affected by both, direct exciton decay and exciton splitting, and by accounting for the exciton lifetime, it is further possible to determine the lifetime of exciton splitting. By considering both, direct exciton decay and exciton splitting at the BHJ interfaces, one can directly determine the exciton splitting efficiency which is a critical parameter in charge generation in organic solar cells.

To fit the TRPL data, it is necessary to use a fitting function which models the decay. Mostly, and in the simplest fashion, the PL decay exhibits an exponentially declining intensity. On a logarithmic scale for PL intensity, which was consistently chosen to plot the TRPL data, an exponential PL decay appears linearly. Inspecting the TRPL data of all polymers (see Supplementary Figure 4a) it becomes apparent that the PL decay indeed is mostly linear over two order of magnitude and specifically in the time regime between 2.6 to 3.4 ns. It is important to note, that at delay times shorter than 2.6 ns the PL signal is strongly non-linear as the PL signal is strongly determined by the pump pulse. In addition, a secondary pump pulse appears at around 3.5 ns which perturbs the PL decay and the apparent linear relationship in Supplementary Figure 4a. This directly demonstrates that it is not possible to perform a fit of the PL decay over the full delay time regime without accounting for the underlying excitation pulse (or instruments response function – IRF). Nevertheless, in the time regime between 2.6 to 3.4 ns it appears that the PL decay is not significantly affected by the underlying IRF. Thus, in Supplementary Figure 4a it is possible to fit e.g. the WF3 decay with an exponential function. The fitting routine yields an exciton decay lifetime of 821 ps, which is significantly longer than the full width half maximum (FWHM) time of the IRF of 150 ps, which is further supporting the validity of the fit. The value of 821 ps can be considered as a robust value for the exciton lifetime in the WF3 layer.

For the acceptors investigated in this study, this fitting routine appears to work decently as well, yielding exciton lifetimes which range from around 300 ps to 1000 ps (Supplementary Figure 4b). In addition, this procedure can also be applied to the PL quenching in WF3FS:eh-IDTBR, yielding a lifetime of 487 ps (Supplementary Figure 4c). However, this PL quenching lifetime in WF3FS:eh-IDTBR is not an exciton lifetime, neither is it the lifetime of exciton splitting. The decay of PL is caused by both mechanism for which reason both lifetimes (or decay rates) must be considered. This is easily understood by the set of following equations:

$$\tau_{measurement} \neq \tau_{exciton\ splitting}$$

$$\frac{1}{\tau_{measurement}} = \frac{1}{\tau_{exciton\ splitting}} + \frac{1}{\tau_{exciton\ decay}}$$

$$k_{measurement} = k_{exciton\ splitting} + k_{exciton\ decay} \quad (1)$$

$$\tau_{exciton\ splitting} = \frac{1}{\frac{1}{\tau_{measurement}} - \frac{1}{\tau_{exciton\ decay}}}$$

In these equations it is briefly shown how the measured PL quenching time and the known exciton lifetime are both used to obtain the lifetime $\tau_{exciton\ splitting}$. Utilizing $\tau_{exciton\ decay} = 885\ ps$ and $\tau_{measurement} = 487\ ps$ this yields $\tau_{exciton\ splitting} = 1083\ ps$. This is intriguing, as the lifetime of exciton splitting exceeds the exciton lifetime. Effectively, this means that more excitons decay back to the ground state in comparison to exciton being splitting at the BHJ interface. By utilizing the following formula,

$$\eta_{exc\ splitting} = \frac{k_{exciton\ splitting}}{k_{exciton\ splitting} + k_{exciton\ decay}}, \tag{2}$$

the efficiency of exciton splitting can directly be quantified. Here, the decay rates *k* are used which are obtained by $k = 1/\tau$. For the case of WF3FS:eh-IDTBR this yields an exciton splitting efficiency of 45 % and thereby demonstrates that photocurrent generation in this blend is strongly limited by poor charge generation.

Yet, for very fast PL decay curves, such as for WF3:eh-IDTBR (Supplementary Figure 4c) or WF3:ITIC (Figure 2c main text), it becomes apparent that the PL decay closely follows the IRF. In such cases it is ill-defined to apply this simple exponential fitting routine. Clearly, any proper fitting routine must consider the influence of the IRF on the PL decay. For this reason, all TRPL data was consistently fitted analysed with the same fitting procedure based on a deconvolution of the TRPL data and the corresponding IRF. Such a fitting routine/software is available with the commercial TRPL setup, which was used to perform all fits. The routine is based on the following formula:

$$PL(t) = \int_{-\infty}^{t} IRF(t') \cdot \sum_{i=1}^{3} e^{-\frac{t-t'}{\tau_i}}\ dt'\ . \tag{3}$$

Here, the time-dependent PL decay is obtained by a convolution of a set of three exponential functions (with the respective fitting parameters) and the IRF. Three exponential functions were necessary to accurately fit the full TRPL decay over more than 3 order of magnitude, as the measured TRPL signal exhibit long tails with significantly less than 1% of the total intensity. For the two examples WF3 and WF3:ITIC the full fits and all details are shown in Supplementary Figures 5 – 10. As for WF3 it is also possible to use the simple fitting routine for comparison, this PL decay is considered first. In Supplementary Figure 5 it is evident that the PL decay is well reproduced by the fit, while the results of the fitting parameters (with quasi negligible fitting errors) are shown in Supplementary Figure 6. In addition, effective average lifetimes for the PL decay are shown in Supplementary Figure 6, with $\boldsymbol{\tau_{avg,1}} = 967$ ps and $\boldsymbol{\tau_{avg,2}} = 575$ ps. It is detected that $\boldsymbol{\tau_{avg,2}}$, which is obtained by weighting $\boldsymbol{\tau_1}$, $\boldsymbol{\tau_2}$ and $\boldsymbol{\tau_3}$ w.r.t. to amplitudes, is significantly shorter than the previously fitted robust value of 821 ps. We reason that a weighting by amplitudes does therefore not yield a reliable result, which makes sense when considering that weighting by amplitudes in a sense only considers time zero. In contrast, the more reasonable weighting via the time-integrated intensities provides an apparently slightly too long lifetime of $\boldsymbol{\tau_{avg,1}} = 967$ ps when compared to 821 ps. This is understood when considering Supplementary Figure 7 in detail. Here it is observed that the exponential function with the longest decay time ($\tau = 3300$ ps) does not contribute to the initial fast decay of PL, but only at PL intensities well below 1 % of the initial PL intensities (which is in the negligible regime when considering solar cell operation). Thus, we reason that the longest lifetime $\tau = 3300$ ps should not be included in the weighted calculation of effective PL decay time $\boldsymbol{\tau_{avg}}$. By using $\boldsymbol{\tau_1}$ and $\boldsymbol{\tau_2}$ we calculate a weighted lifetime of 829 ps for the TRPL signal of WF3, which is fully in line with the 821 ps obtained via the simple robust fitting routine (see Supplementary Figure 4a).

While this analysis routine based on the weighting of $\boldsymbol{\tau_1}$ and $\boldsymbol{\tau_2}$ works very well for WF3, it does not work well for very fast PL decays such as for WF3:ITIC. This becomes apparent when considering Supplementary Figures 8 – 10. Especially considering Supplementary Figure 10, it is seen that the very fast PL quenching (to 1% intensity) is entirely described by the fastest exponential decay function. For this reason, only the fastest lifetime $\boldsymbol{\tau_1}$ = 24.8 ps is considered for WF3:ITIC (any weighting with $\boldsymbol{\tau_1}$ and $\boldsymbol{\tau_2}$ leads to clearly wrong values for exciton splitting efficiencies – not shown). Thus, only $\boldsymbol{\tau_1}$ is used for very fast PL decays. Empirically, only $\boldsymbol{\tau_1}$ is used as effective lifetime if the corresponding amplitude is higher than 95 % compared to the sum of amplitudes. Otherwise, $\boldsymbol{\tau}_{avg}$ is calculated by weighting $\boldsymbol{\tau_1}$ and $\boldsymbol{\tau_2}$.

Based on these fitting routine, all exciton lifetimes and PL quenching lifetimes are calculated and listed in Supplementary Table 1. By further utilizing Supplementary Equations 1 and 2, the lifetime of exciton splitting and the exciton splitting efficiency are calculated for each blend, see Supplementary Table 2.

Model: Exp. [Reconv.] (Exponential)
Plotted Data Set #0 Decay: "\..\Decay+IRF_20190717_1446.etf" (1)
Plotted Data Set #0 IRF: "\..\Decay+IRF_20190717_1446.etf" (0)
X²(reduced): 2.3246 ; Fitted Data Points: 1413

Main Plot

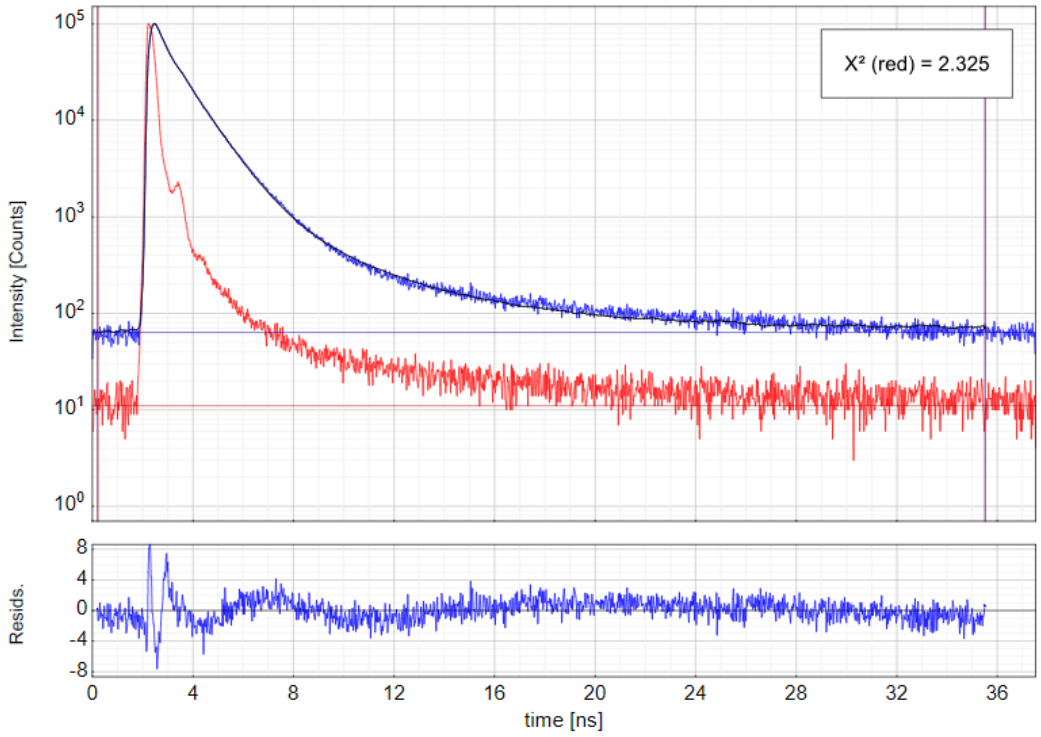

$$I(t) = \int_{-\infty}^{t} IRF(t') \sum_{i=1}^{n} A_i \, e^{-\frac{t-t'}{\tau_i}} \, dt'$$

Supplementary Figure 5 | Fit of the TRPL of WF3 with commercial Fluofit software. To obtain a high quality of the fit, a sum of three exponential functions was used and the software internally convolutes the fit function (three exponentials) with the excitation pulse (instruments response function – IRF, in red color) which was measured separately. See Supplementary Note 1 for details.

Parameter	Value	Conf. Lower	Conf. Upper	Conf. Estimation
A_1 [Cnts]	2106.8	-88.0	+88.0	Fitting
τ_1 [ns]	3.3202	-0.0716	+0.0716	Fitting
A_2 [Cnts]	95561	-508	+508	Fitting
τ_2 [ns]	0.99433	-0.00388	+0.00388	Fitting
A_3 [Cnts]	123270	-2020	+2020	Fitting
τ_3 [ns]	0.20243	-0.00351	+0.00351	Fitting
Bkgr. Dec [Cnts]	63.37	-2.65	+2.65	Fitting
Bkgr. IRF [Cnts]	11.0	---	---	<none>
Shift IRF [ns]	0.02496	-0.00111	+0.00111	Fitting

Average Lifetime:

$\tau_{Av.1}$=0.9668 ns (intensity weighted)

$\tau_{Av.2}$=0.5747 ns (amplitude weighted)

Fractional Intensities of the Positive Decay Components:

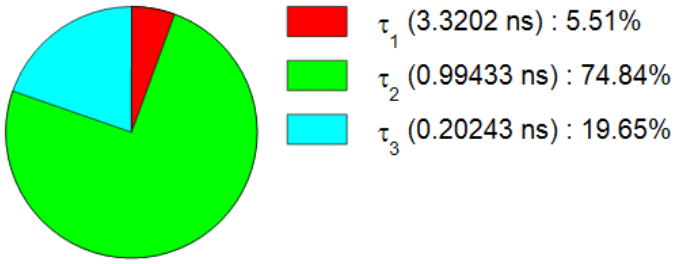

Fractional Amplitudes of the Positive Decay Components:

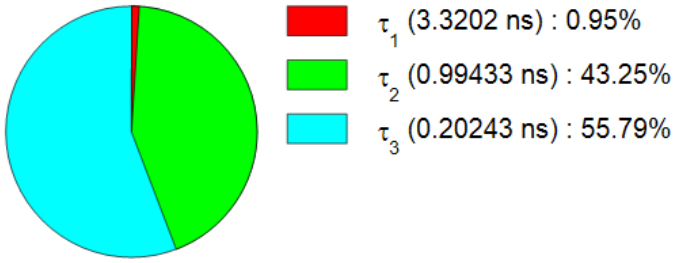

Supplementary Figure 6 | Parameters of the fit of the TRPL of WF3 with commercial Fluofit software. The upper table shows fitted parameters. Futher, average lifetimes $\boldsymbol{\tau_{avg,1}}$ and $\boldsymbol{\tau_{avg,2}}$ are given based on a weighting of fitted lifetimes $\boldsymbol{\tau_1}$, $\boldsymbol{\tau_2}$ and $\boldsymbol{\tau_3}$. The latter lifetimes are used to determine PL quenching lifetime, see Supplementary Note 1.

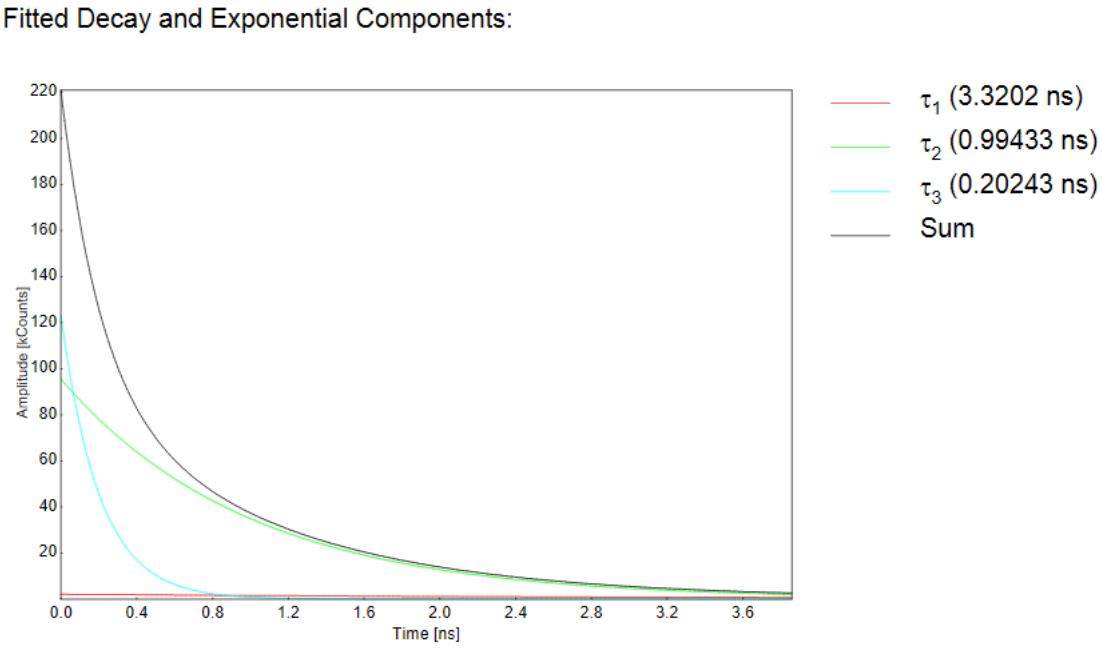

Supplementary Figure 7 | Visualization of the fit of the TRPL of WF3 with commercial Fluofit software. The individual contributions of the three exponential fit functions to the overall PL decay is shown. It is seen that the exponential fit function with the longest lifetime (corresponds to red curve in upper panel) is negligible regarding the initial fast decay. See Supplementary Note 1 for more details.

Model: Exp. [Reconv.] (Exponential)
Plotted Data Set #0 Decay: "\..\Decay+IRF_20190712_1406.etf" (1)
Plotted Data Set #0 IRF: "\..\Decay+IRF_20190712_1406.etf" (0)
X²(reduced): 1.7057 ; Fitted Data Points: 932

Main Plot

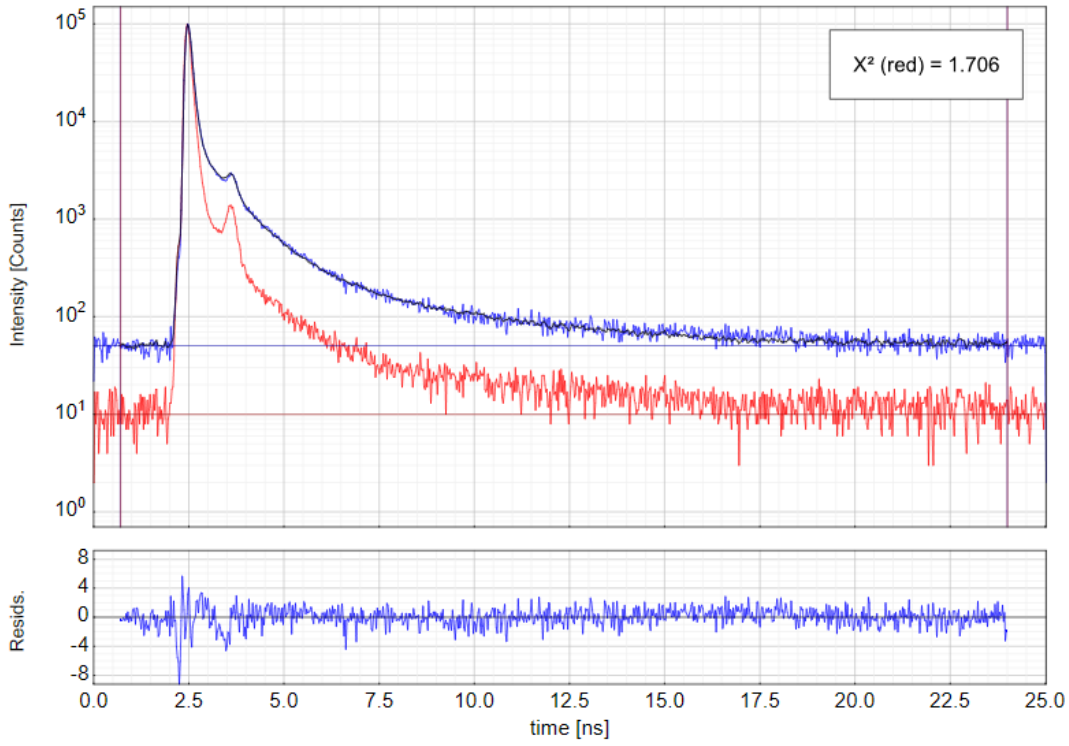

$$I(t) = \int_{-\infty}^{t} IRF(t') \sum_{i=1}^{n} A_i \, e^{-\frac{t-t'}{\tau_i}} \, dt'$$

Supplementary Figure 8 | Fit of the TRPL of WF3:ITIC with commercial Fluofit software. To obtain a high quality of the fit, a sum of three exponential functions was used and the software internally convolutes the fit function (three exponentials) with the excitation pulse (instruments response function – IRF, in red color) which was measured separately. See Supplementary Note 1 for details.

Parameter	Value	Conf. Lower	Conf. Upper	Conf. Estimation
A_1 [Cnts]	371.2	-21.4	+21.4	Fitting
τ_1 [ns]	3.297	-0.132	+0.132	Fitting
A_2 [Cnts]	5239	-132	+132	Fitting
τ_2 [ns]	0.7606	-0.0140	+0.0140	Fitting
A_3 [Cnts]	1475800	-10700	+10700	Fitting
τ_3 [ns]	0.024777	-0.000113	+0.000113	Fitting
Bkgr. Dec [Cnts]	50.23	-1.90	+1.90	Fitting
Bkgr. IRF [Cnts]	10.0	---	---	<none>
Shift IRF [ns]	0.005656	-0.000612	+0.000612	Fitting

Average Lifetime:

$\tau_{Av.1}$=0.191 ns (intensity weighted)

$\tau_{Av.2}$=0.0282 ns (amplitude weighted)

Fractional Intensities of the Positive Decay Components:

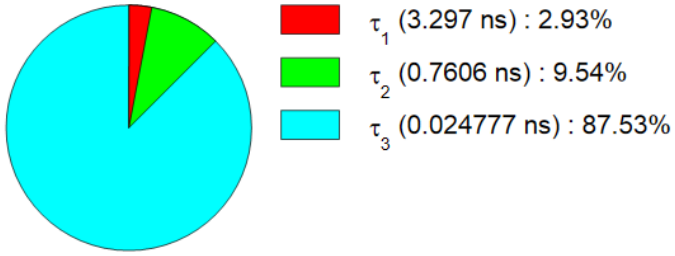

Fractional Amplitudes of the Positive Decay Components:

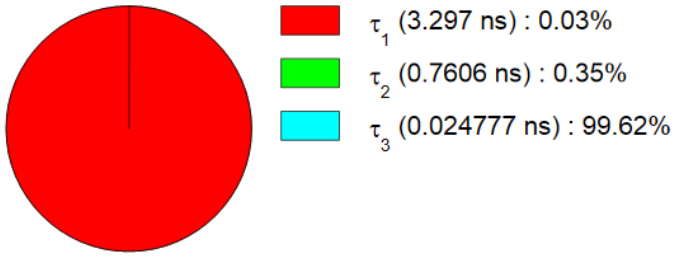

Supplementary Figure 9 | Parameters of the fit of the TRPL of WF3:ITIC with commercial Fluofit software. The upper table shows fitted parameters. Futher, average lifetimes $\boldsymbol{\tau_{avg,1}}$ and $\boldsymbol{\tau_{avg,2}}$ are given based on a weighting of fitted lifetimes $\boldsymbol{\tau_1}$, $\boldsymbol{\tau_2}$ and $\boldsymbol{\tau_3}$. The latter lifetimes are used to determine PL quenching lifetime, see Supplementary Note 1.

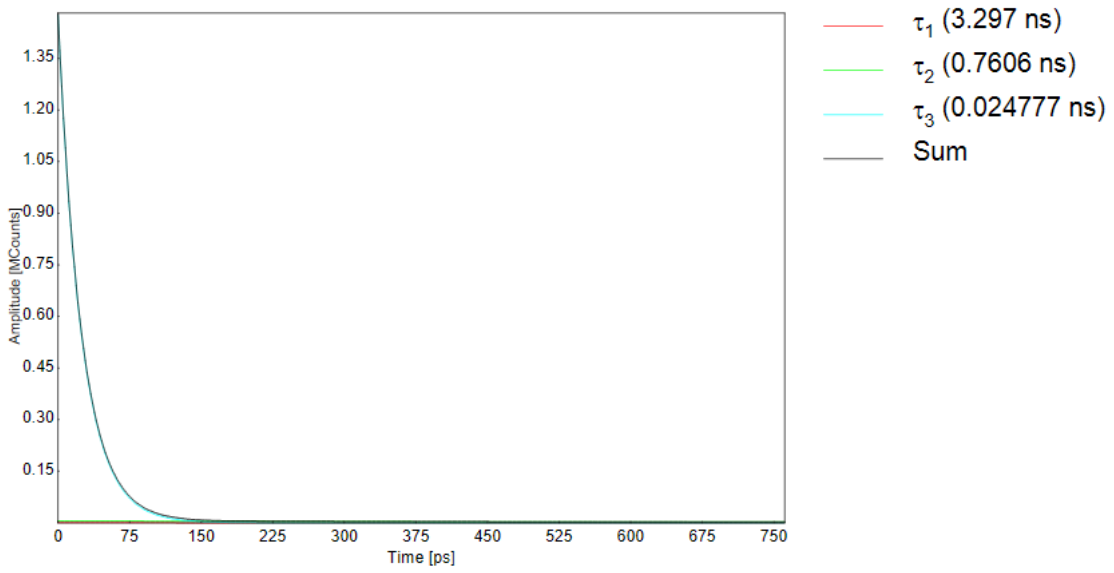

Confidence Intervals:

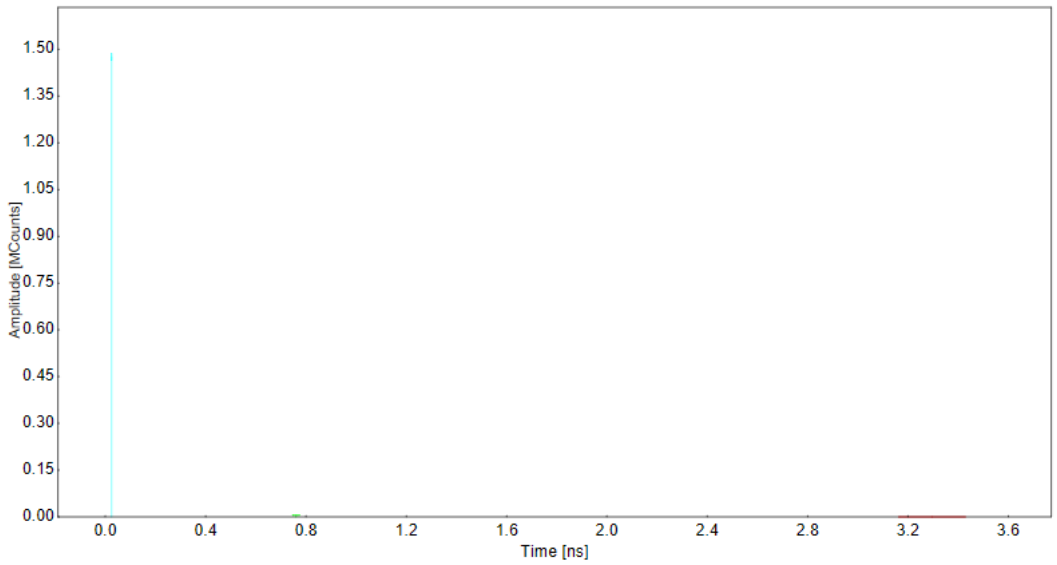

Supplementary Figure 10 | Visualization of the fit of the TRPL of WF3:ITIC with commercial Fluofit software. The individual contributions of the three exponential fit functions to the overall PL decay is shown. It is seen that only the exponential fit function with the shortest lifetime (corresponds to teal curve in upper panel) contributes to the initial fast decay. See Supplementary Note 1 for more details.

Supplementary Table 1: All lifetimes relevant for the evaluation of exciton splitting efficiencies (see Supplementary Table S2) and the detailed results of the fitting parameters obtained via the commercial software fitting routine, see Supplementary Figures 5 – 10 for fits of WF3 and WF3:ITIC and Supplementary Note1 for a detailed description of the fitting routine.The fitting routine is based on a deconvolution of the IRF and a triple-exponential fit with corresponding lifetimes $\boldsymbol{\tau_1}$, $\boldsymbol{\tau_2}$ and $\boldsymbol{\tau_3}$, which are given in picoseconds. For very fast PL decays (WF3:ITIC) only $\boldsymbol{\tau_1}$ is used. Otherwise, a weighting based on $\boldsymbol{\tau_1}$ and $\boldsymbol{\tau_2}$ is performed by using the relative integrated Intensities of the respective exponential functions (Int_1 and Int_2). The relative Amplitudes (A_1 and A_2) are not used. All exciton lifetimes used for additional analysis are highlighted in red color. The lifetimes related to the "manual fit" based on a simple mono-exponential function, see Supplementary Figure 4, show very similar results.

	τ_{avg} (ps)	τ_1 (ps)	A_1 (%)	Int_1 (%)	τ_2 (ps)	A_2 (%)	Int_2 (%)	τ_3 (ps)	A_3 (%)	Int_3 (%)	"manual fit" (ps)
WF3	**829.4**	**202.4**	0.558	**0.197**	**994**	0.433	**0.748**	3320	0.010	0.055	821.4
ITIC	**305.3**	**151.7**	0.896	**0.643**	**634**	0.100	**0.300**	2850	0.004	0.057	309.1
Y6	**1016**	**608.9**	0.651	**0.408**	**1305**	0.349	**0.576**	22860	0.001	0.016	1049.5
eh-IDTBR	**898.3**	**278.9**	0.594	**0.259**	**1125**	0.402	**0.706**	5060	0.004	0.035	884.7
o-IDTBR	**561.5**	**316.4**	0.783	**0.547**	**882**	0.214	**0.419**	4328	0.004	0.035	530.2
WF3:ITIC	97.0	**24.7**	0.996	0.875	760	0.004	0.095	3297	0.000	0.029	x
WF3S:ITIC	109.5	**27.4**	0.995	0.850	721	0.005	0.114	3204	0.000	0.036	x
WF3F:ITIC	109.4	**29.7**	0.994	0.846	698	0.006	0.115	2851	0.001	0.040	x
WF3FS:ITIC	186.2	**47.5**	0.975	0.691	635	0.023	0.214	3053	0.002	0.095	x
WF3:Y6	87.5	**29.0**	0.974	0.720	303	0.025	0.196	5920	0.001	0.084	x
WF3S:Y6	88.9	**27.4**	0.977	0.728	324	0.023	0.190	6031	0.001	0.082	x
WF3F:Y6	86.7	**39.1**	0.983	0.800	401	0.016	0.121	4017	0.001	0.079	x
WF3FS:Y6	89.1	**41.2**	0.981	0.795	398	0.018	0.123	4052	0.001	0.081	x
WF3:eh-IDTBR	99.6	**39.9**	0.985	0.794	470	0.014	0.128	1962	0.002	0.080	x
WF3S:eh-IDTBR	169.2	**50.8**	0.974	0.700	588	0.024	0.198	2862	0.003	0.102	x
WF3F:eh-IDTBR	**174.4**	**73.9**	0.875	**0.552**	**329**	0.120	**0.359**	1965	0.005	0.090	x
WF3FS:eh-IDTBR	**499.1**	**217.0**	0.791	**0.473**	**816**	0.199	**0.421**	3847	0.011	0.107	487.3
WF3:o-IDTBR	50.5	**24.5**	0.993	0.858	341	0.006	0.077	1733	0.001	0.065	x
WF3S:o-IDTBR	195.1	**54.8**	0.976	0.705	644	0.023	0.221	4197	0.001	0.074	x
WF3F:o-IDTBR	**183.9**	**70.8**	0.934	**0.630**	**443**	0.062	**0.275**	2856	0.004	0.095	x
WF3FS:o-IDTBR	**398.8**	**183.7**	0.807	**0.507**	**658**	0.187	**0.421**	3194	0.007	0.073	372.0

Supplementary Table 2: (same as Table 1 in the main text). Calculation of the efficiency of exciton splitting based on the lifetimes listed in Supplementary Table 1, by using Supplementary Equations 1 and 2. See Supplementary Note 1 for details. All lifetimes are given in picoseconds and exciton splitting efficiencies are given in %.

	Exciton lifetimes (ps)
ITIC	305.3
Y6	1016
eh-IDTBR	898.3
o-IDTBR	561.5

	PL quenching Lifetimes (ps)	Exciton splitting Lifetimes (ps)	Efficiency of exciton Splitting (%)
WF3:ITIC	24.7	26.9	0.919
WF3S:ITIC	27.4	30.1	0.910
WF3F:ITIC	29.7	32.9	0.903
WF3FS:ITIC	47.5	56.3	0.844
WF3:Y6	29.0	29.9	0.971
WF3S:Y6	27.4	28.2	0.973
WF3F:Y6	39.1	40.7	0.962
WF3FS:Y6	41.2	42.9	0.959
WF3:eh-IDTBR	39.9	41.8	0.956
WF3S:eh-IDTBR	50.8	53.8	0.943
WF3F:eh-IDTBR	174.4	216.4	0.806
WF3FS:eh-IDTBR	499.1	1123.1	0.444
WF3:o-IDTBR	24.5	25.6	0.956
WF3S:o-IDTBR	54.8	60.7	0.902
WF3F:o-IDTBR	183.9	273.5	0.672
WF3FS:o-IDTBR	398.8	1376.7	0.290

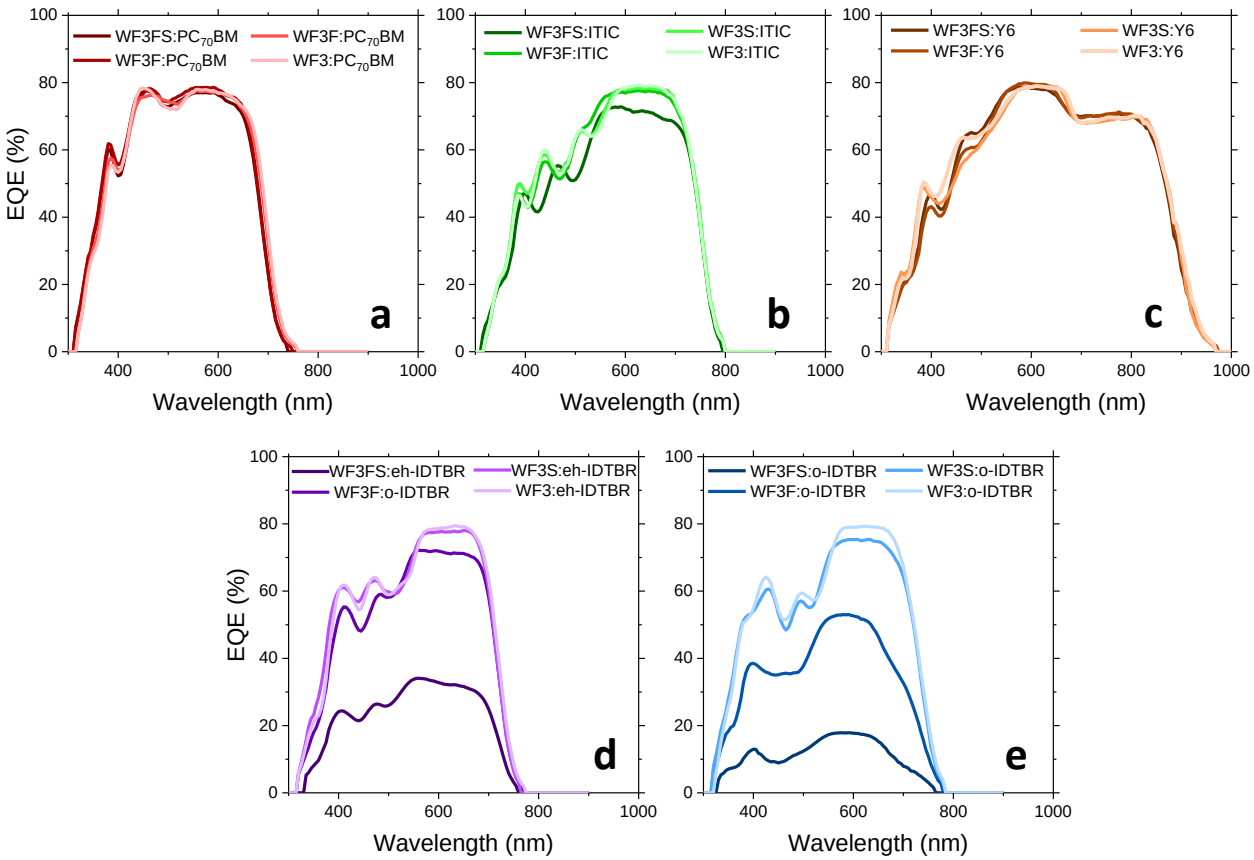

Supplementary Figure 11 | EQE spectra of all solar cells investigated in this work. a) of all $PC_{70}BM$ based devices, **b)** of all ITIC based devices, **c)** of all Y6 based devices, **d)** of all eh-IDTBR based devices and **e)** of all o-IDTBR based devices.

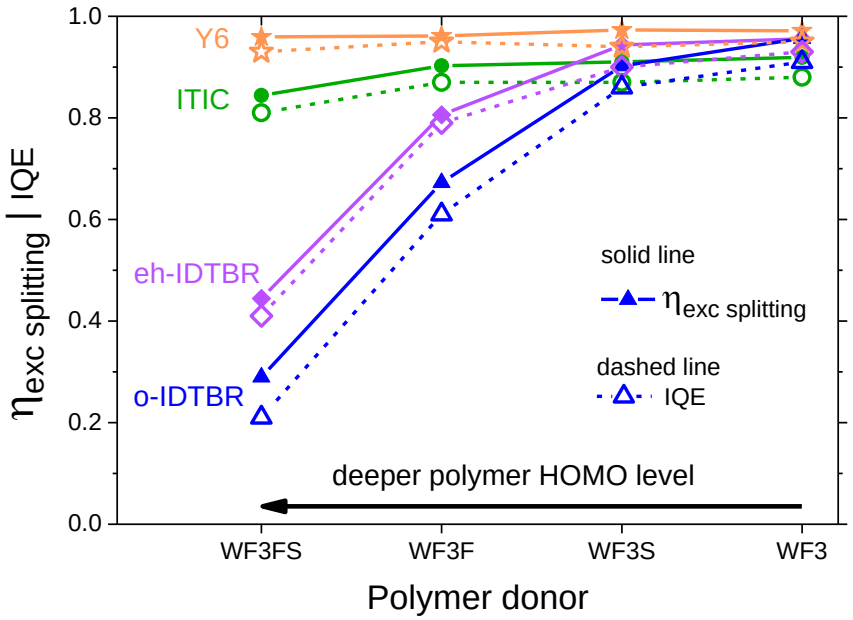

Supplementary FigureS12 | Exciton splitting efficiency and its correlation with internal quantum efficiency. Exciton splitting efficiency is derived from TRPL measurements and IQE of devices is shown in Supplementary Figures 13 – 16.

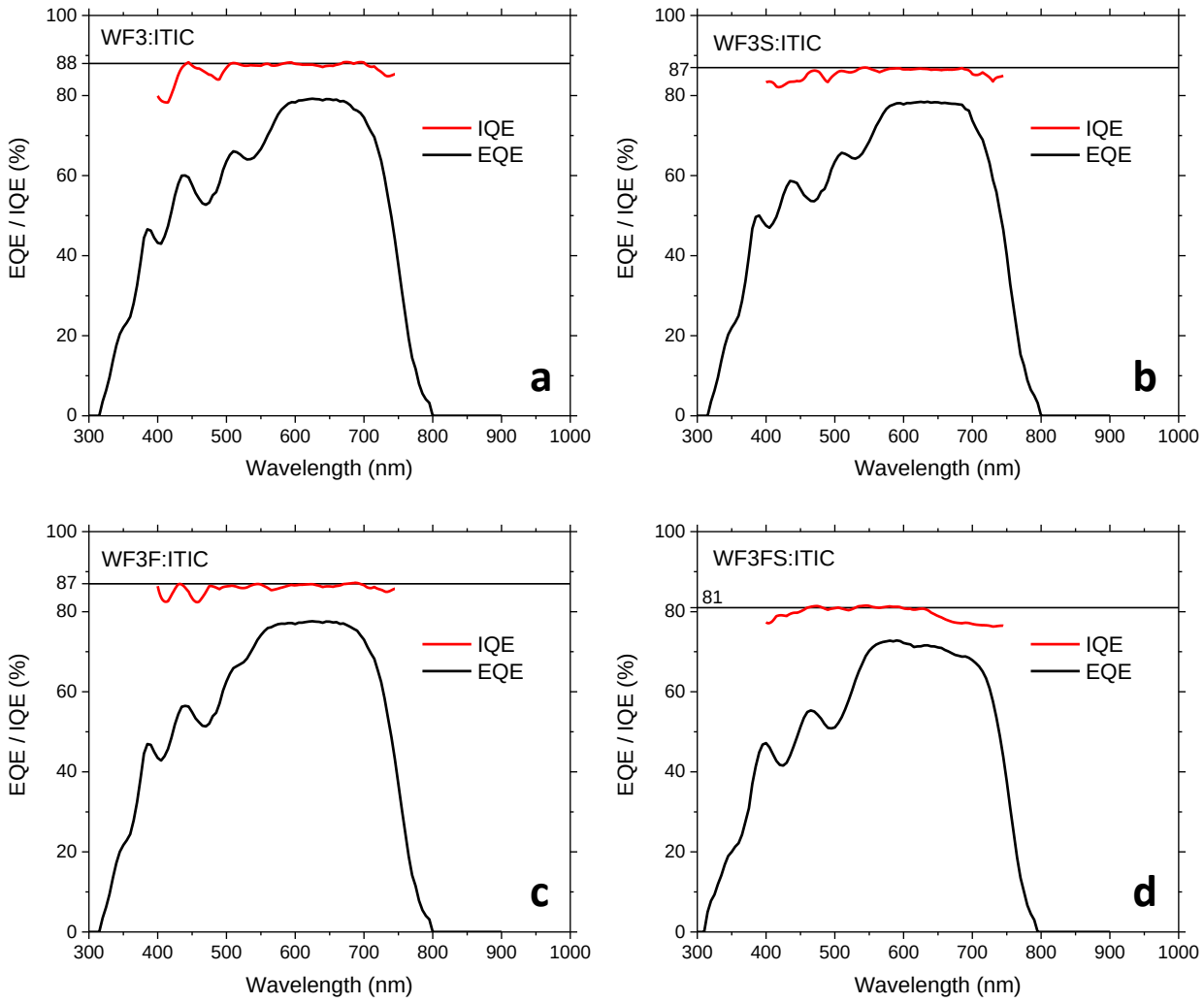

Supplementary Figure 13 | Internal quantum efficiency. IQE of ITIC based devices calculated using a full transfer matrix model. See Methods for details.

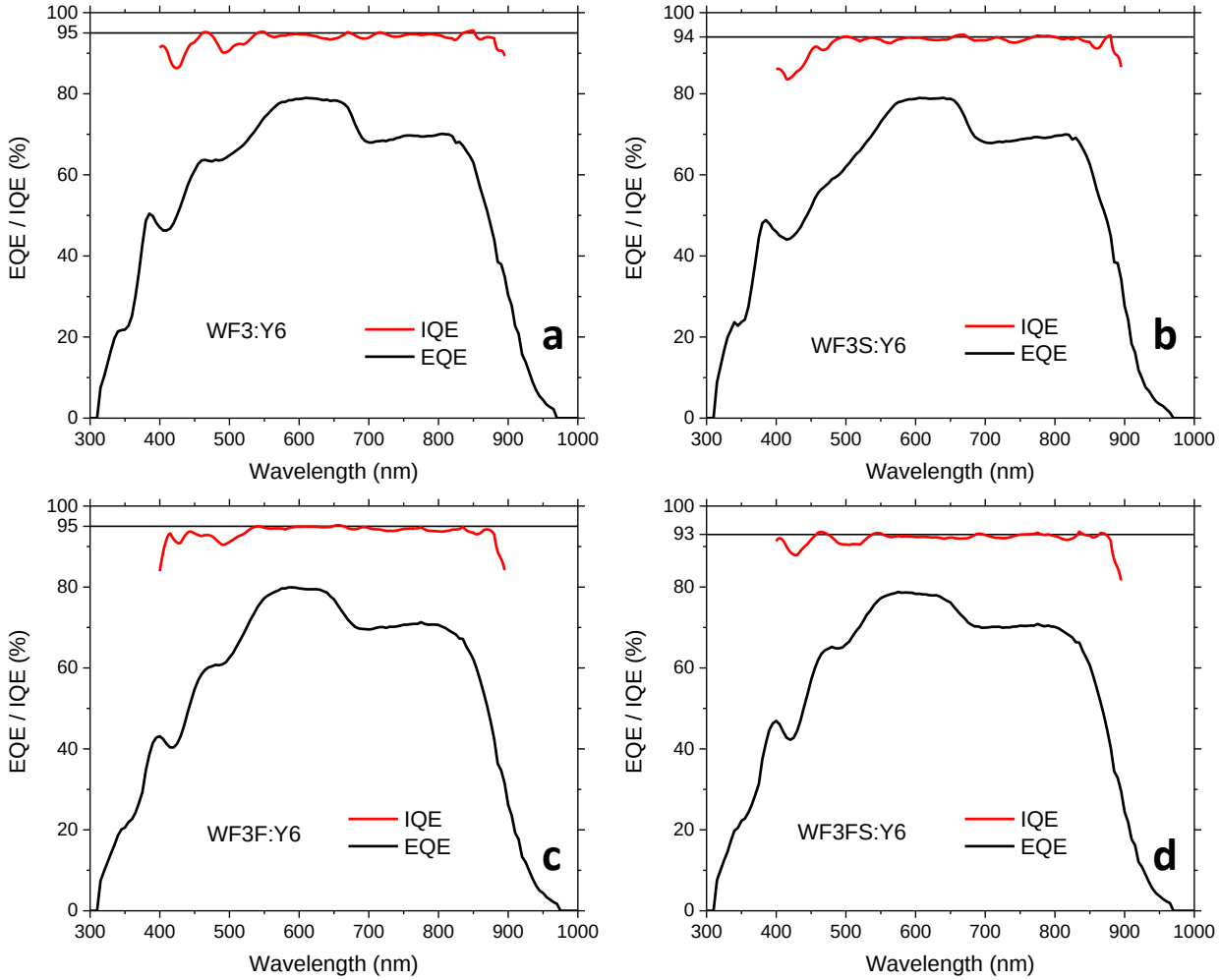

Supplementary Figure 14 | Internal quantum efficiency. IQE of Y6 based devices calculated using a full transfer matrix model. See Methods for details.

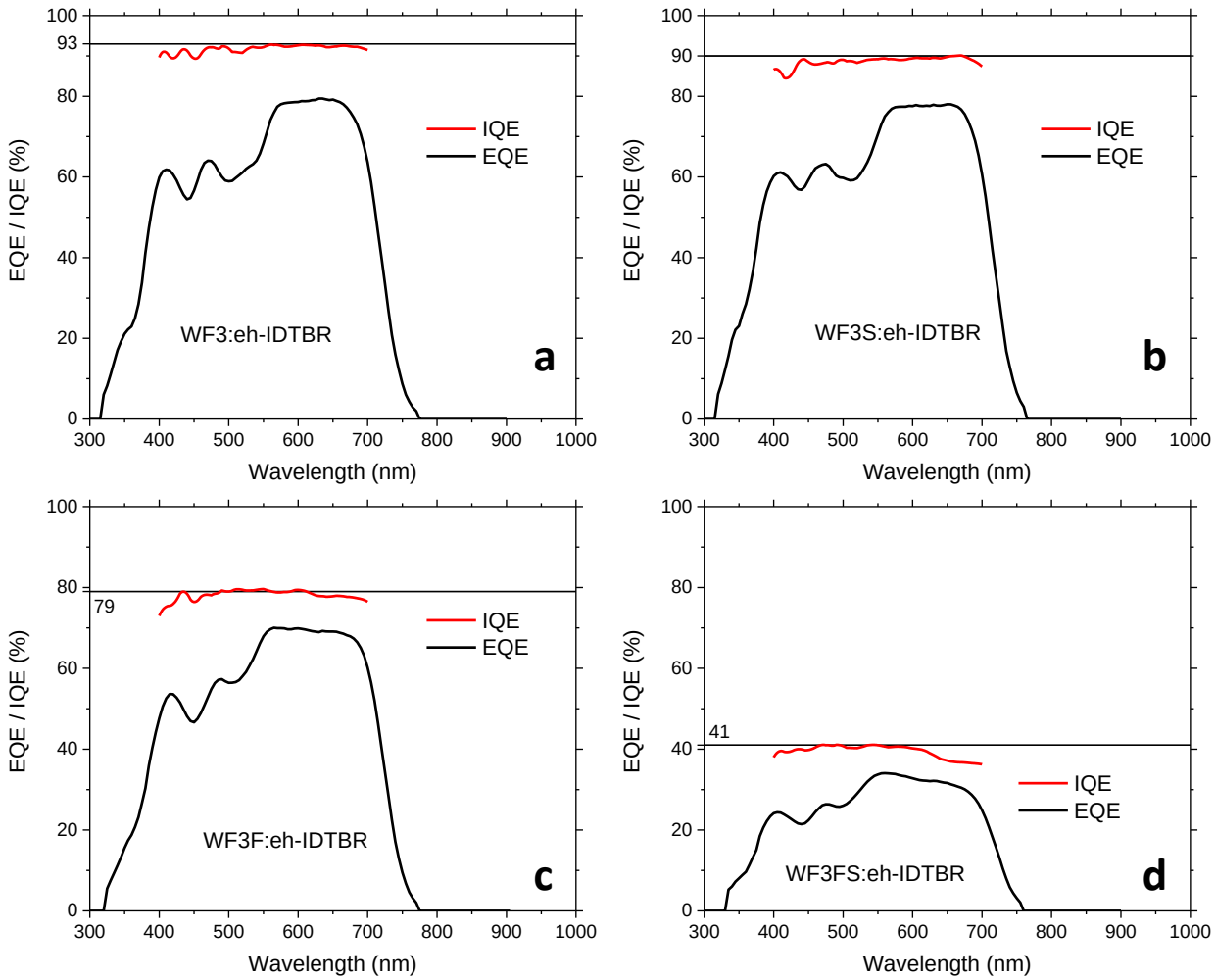

Supplementary Figure 15 | Internal quantum efficiency. IQE of eh-IDTBR based devices calculated using a full transfer matrix model. See Methods for details.

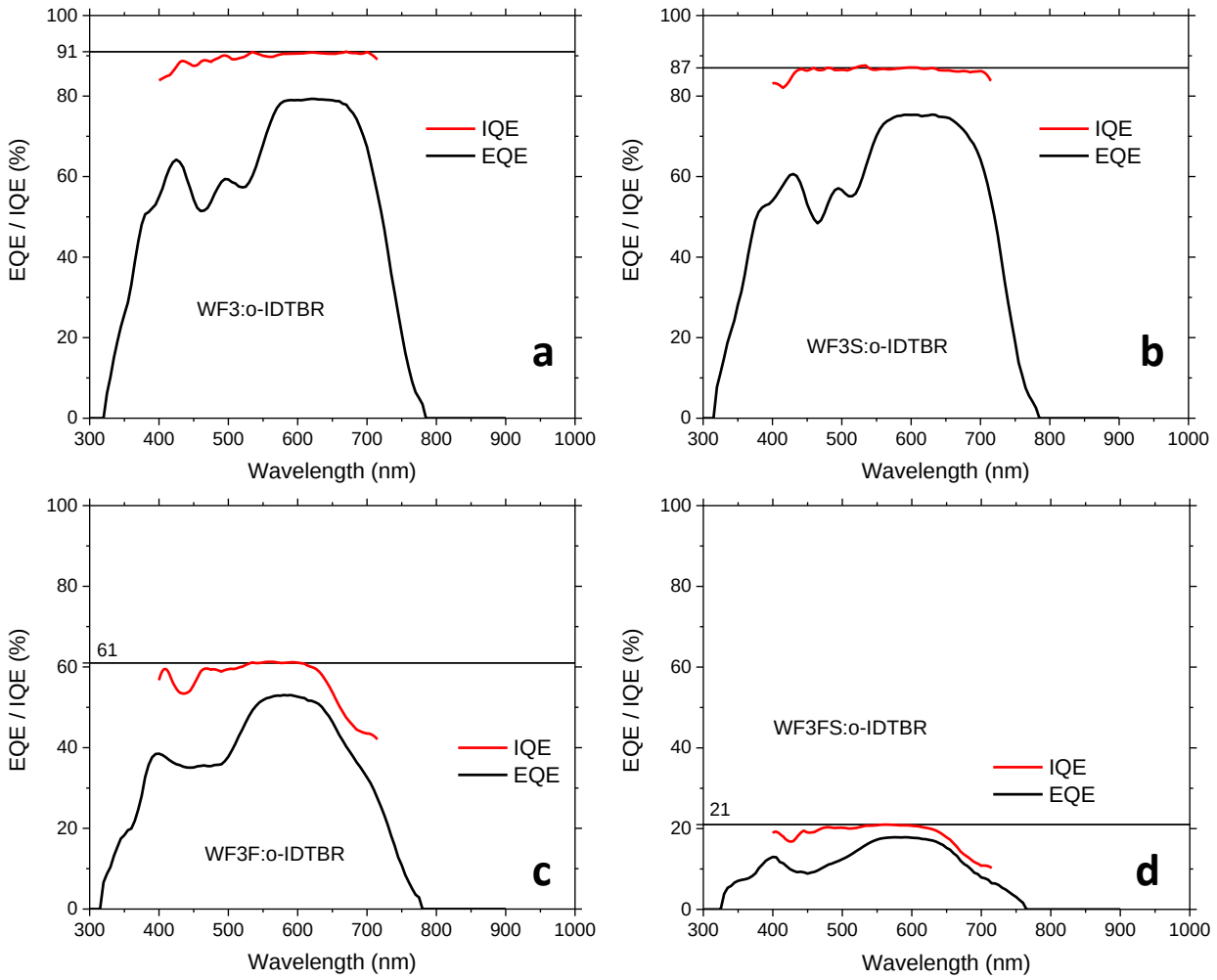

Supplementary Figure 16 | Internal quantum efficiency. IQE of o-IDTBR based devices calculated using a full transfer matrix model. See Methods for details.

Supplementary Table 3 | Parameters of *J-V* characteristics of all solar cells. See Figures 4a – 4e main text for *J-V* curves. The results are based on at least 12 solar cells for each type and the deviation in V_{OC} is shown in parentheses.

	J_{SC}	V_{OC}	FF	PCE
WF3:$PC_{70}BM$	14.70	**0.782 (0.773 ± 0.008)**	65.8	7.56
WF3S:$PC_{70}BM$	14.91	**0.858 (0.851 ± 0.011)**	66.1	8.45
WF3F:$PC_{70}BM$	14.52	**0.892 (0.883 ± 0.015)**	66.9	8.71
WF3FS:$PC_{70}BM$	14.32	**0.959 (0.952 ± 0.007)**	63.8	8.80
WF3:ITIC	16.75	**0.832 (0.827 ± 0.008)**	62.6	8.74
WF3S:ITIC	16.72	**0.897 (0.890 ± 0.013)**	63.1	9.46
WF3F:ITIC	16.77	**0.941 (0.933 ± 0.009)**	65.1	10.31
WF3FS:ITIC	15.75	**1.001 (0.990 ± 0.012)**	54.3	8.56
WF3:Y6	22.25	**0.701 (0.697 ± 0.009)**	61.9	9.65
WF3S:Y6	21.95	**0.741 (0.734 ± 0.011)**	62.9	10.24
WF3F:Y6	22.33	**0.792 (0.788 ± 0.006)**	65.2	11.55
WF3FS:Y6	22.51	**0.839 (0.835 ± 0.007)**	62.8	11.87
WF3:eh-IDTBR	15.26	**1.030 (1.022 ± 0.013)**	61.3	9.65
WF3S:eh-IDTBR	14.96	**1.081 (1.075 ± 0.009)**	59.6	9.64
WF3F:eh-IDTBR	14.30	**1.128 (1.122 ± 0.007)**	57.6	9.29
WF3FS:eh-IDTBR	6.50	**1.161 (1.158 ± 0.007)**	40.8	3.08
WF3:o-IDTBR	16.00	**1.012 (1.004 ± 0.011)**	58.4	9.47
WF3S:o-IDTBR	14.97	**1.051 (1.043 ± 0.009)**	54.0	8.49
WF3F:o-IDTBR	11.25	**1.110 (1.105 ± 0.009)**	51.4	6.42
WF3FS:o-IDTBR	2.99	**1.121 (1.116 ± 0.007)**	35.8	1.20

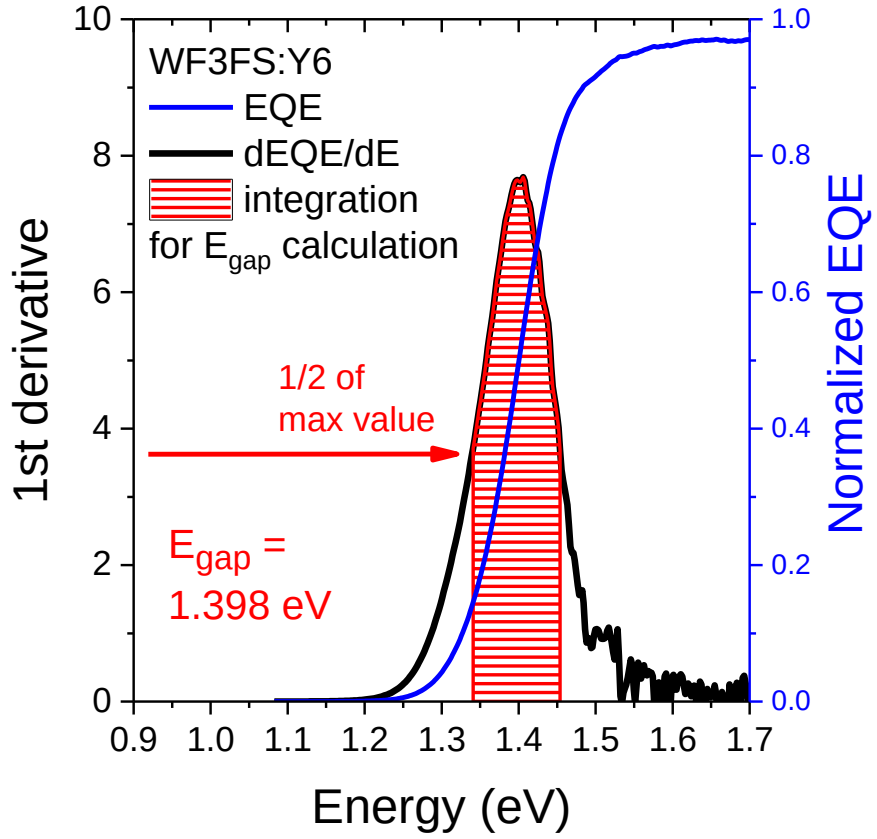

Supplementary Figure 17 | Calculation of photovoltaic bang gap E_{gap}. The calculation is based on the methodology reported in ref[1]. This example is performed for WF3FS:Y6.

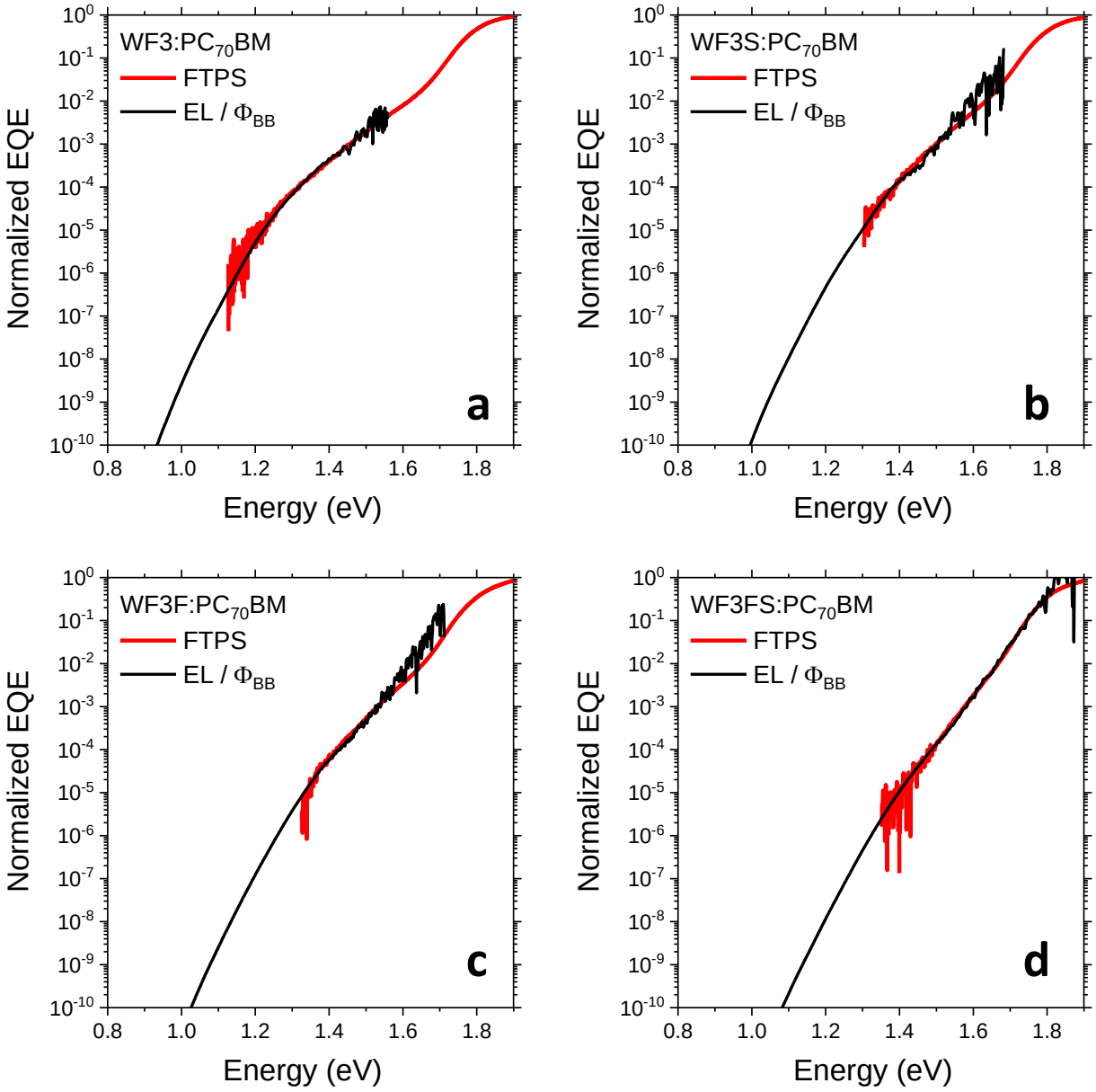

Supplementary Figure 18 | Alignment of EL and EQE to calculate the radiative V_{OC}. For **a)** WF3: $PC_{70}BM$, **b)** WF3S: $PC_{70}BM$, **c)** WF3F: $PC_{70}BM$ and **d)** WF3FS: $PC_{70}BM$.

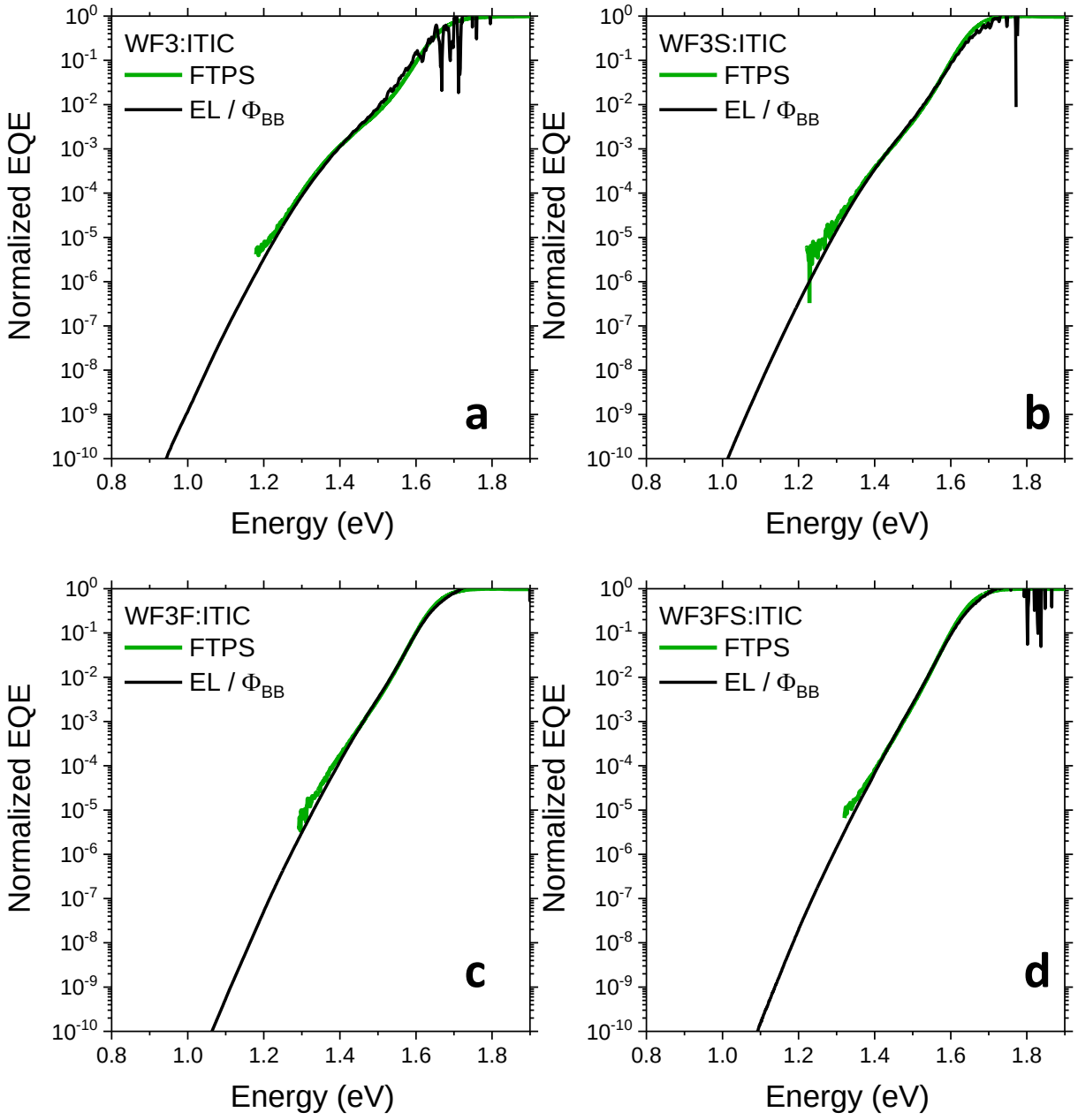

Supplementary Figure 19 | Alignment of EL and EQE to calculate the radiative V_{OC}. For **a)** WF3:ITIC, **b)** WF3S: ITIC, **c)** WF3F: ITIC and **d)** WF3FS: ITIC.

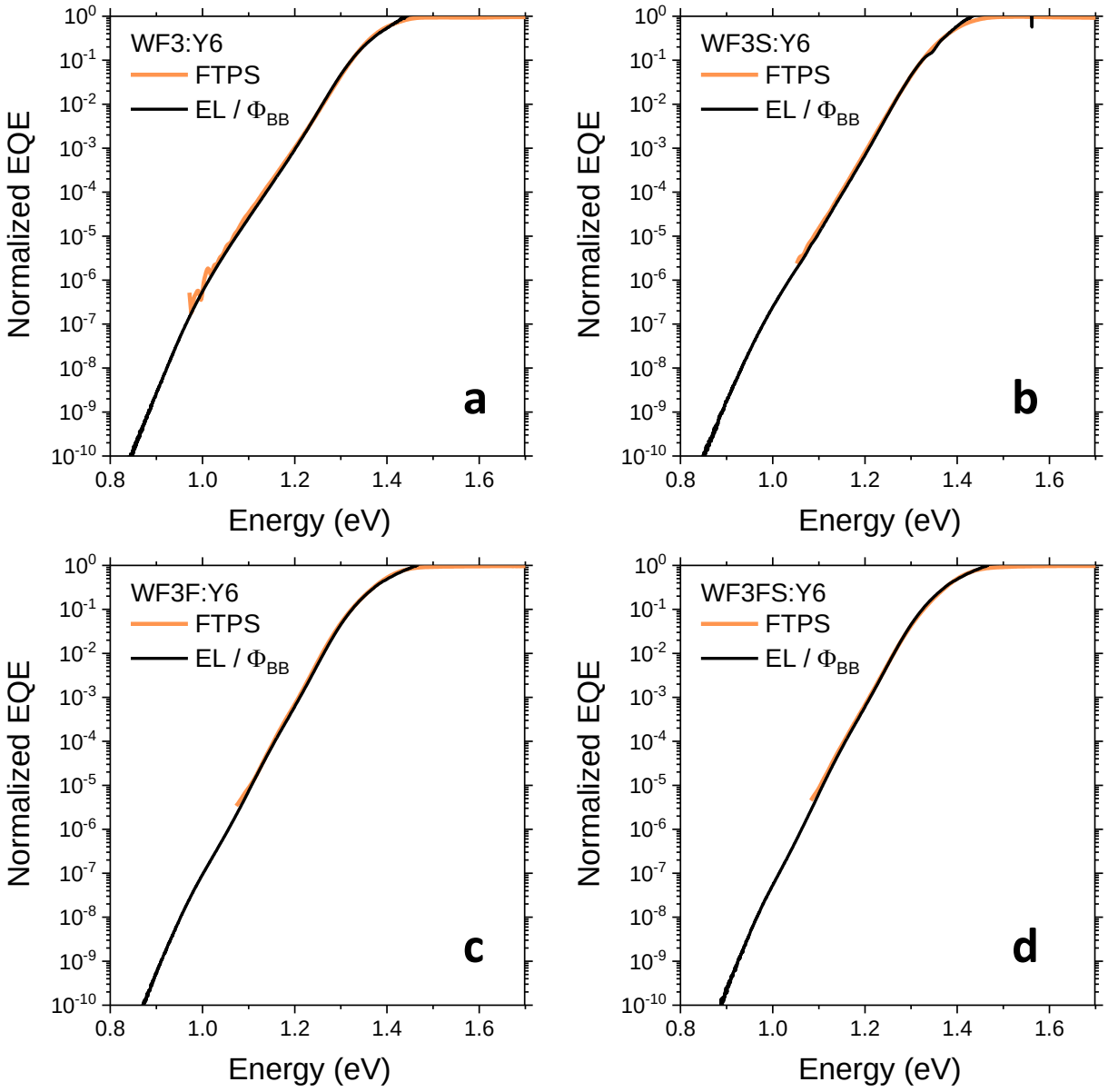

Supplementary Figure 20 | Alignment of EL and EQE to calculate the radiative V_{OC}. For **a)** WF3:Y6, **b)** WF3S:Y6, **c)** WF3F:Y6 and **d)** WF3FS:Y6.

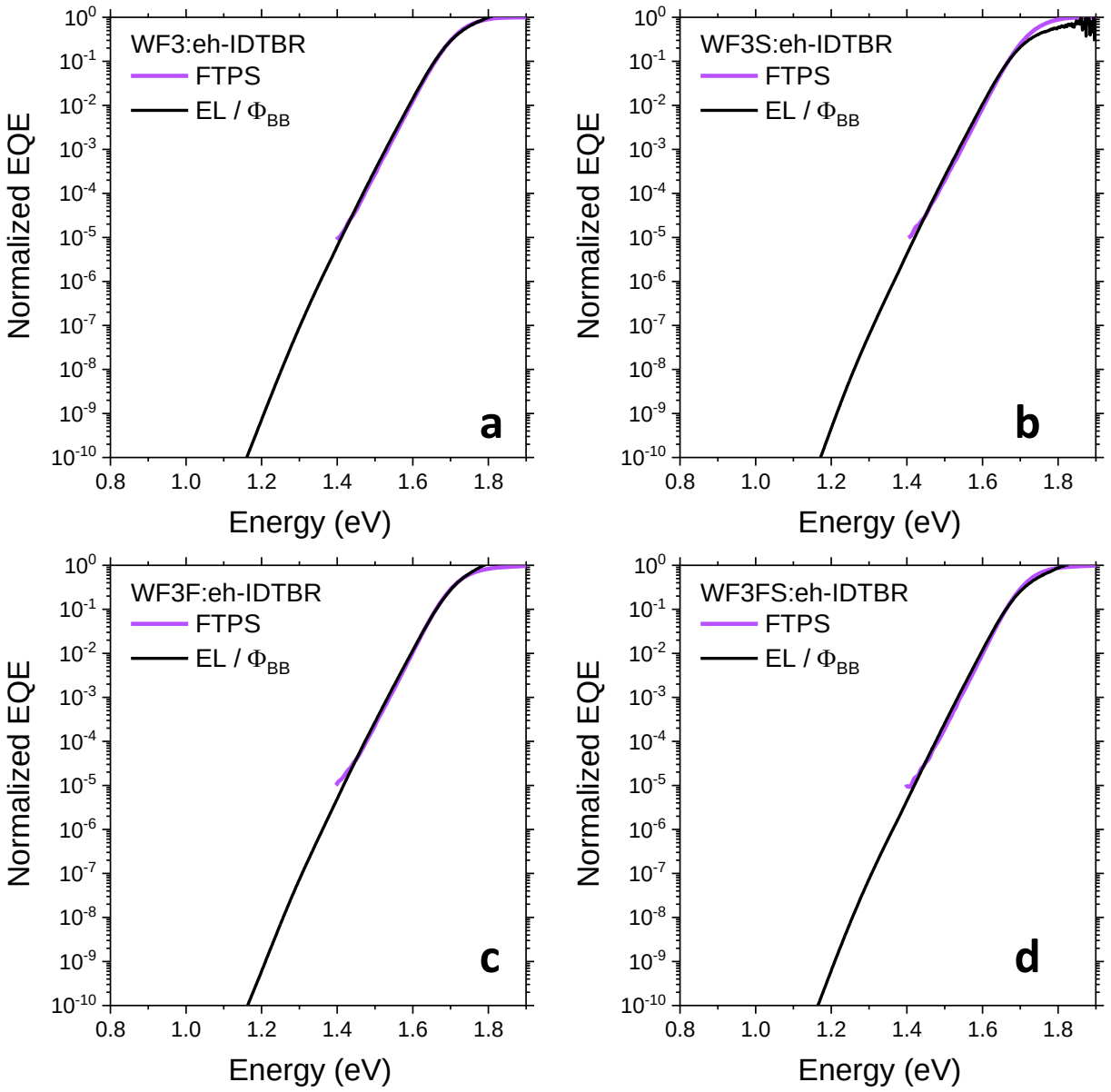

Supplementary Figure 21 | Alignment of EL and EQE to calculate the radiative V_{OC}. For **a)** WF3:eh-IDTBR, **b)** WF3S:eh-IDTBR, **c)** WF3F:eh-IDTBR and **d)** WF3FS:eh-IDTBR.

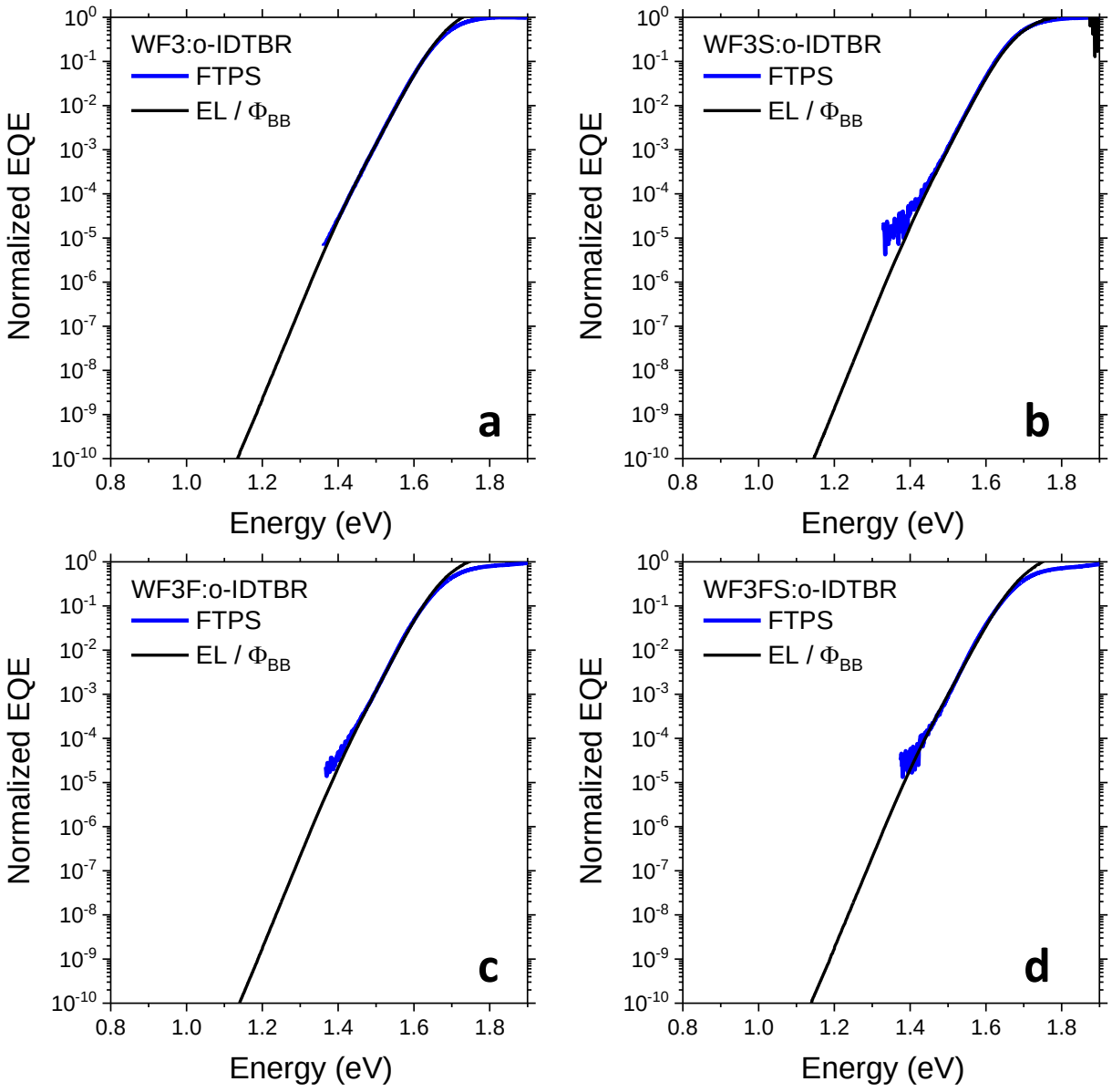

Supplementary Figure 22 | Alignment of EL and EQE to calculate the radiative V_{OC}. For **a)** WF3:o-IDTBR, **b)** WF3S:o-IDTBR, **c)** WF3F:o-IDTBR and **d)** WF3FS:o-IDTBR.

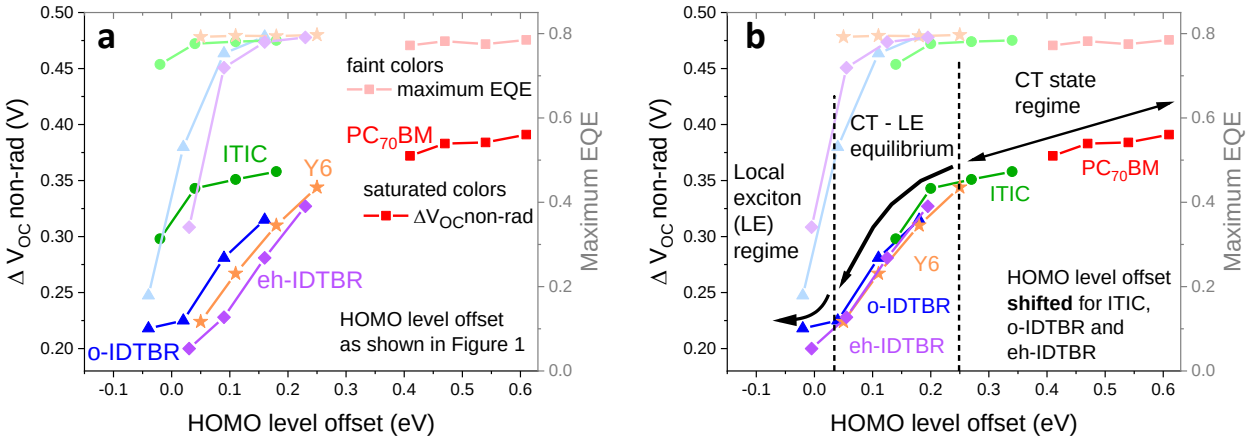

Supplementary Figure 23 | $\Delta V_{OC,non\text{-}rad}$ and maximum EQE of all solar cells with respect to the HOMO level offset. a) With E_{HOMO} of pristine material acceptors, as shown in Figure 1b in the main text, which is based on literature values. Since CV measurement demonstrate that in BHJ solar cells energy levels may shift drastically[2], as for example in WF3:ITIC (Supplementary Figure 2), E_{HOMO} were shifted in **b)** to align $\Delta V_{OC,non\text{-}rad}$ for the NFAs which allows for a direct intersystem comparison of maximum EQE at equal $\Delta V_{OC,non\text{-}rad}$. We observe that Y6 can maintain an excellent EQE despite the minimal $\Delta V_{OC,non\text{-}rad}$. Further, this alignment reveals the trend of a strongly decreasing $\Delta V_{OC,non\text{-}rad}$ when the energy level offset is tuned to small values.

Supplementary Note 2: Analytical description of the LE ⇔ CT equilibrium

If the CT stabilization energies $\Delta E_{LE,CT}$ approach the thermal energy k_BT, then an equilibrium between LE and CT states must be considered.[3,4] This equilibrium causes presence of LE states throughout the lifetime of CT states. The smaller $\Delta E_{LE,CT}$, the more this equilibrium will be on the LE side, so that for vanishing driving forces, the relaxation behavior of LE states becomes important for the description of EQE and $\Delta V_{OC,nr}$.
In the following we show that ***all key aspects*** of this paper are a ***direct consequence*** of this LE ⇔ CT equilibrium, namely

- the increasing exciton lifetime for smaller driving forces (**Figure 2 of main text**)
- the reduction of IQE with decreasing $\Delta E_{LE,CT}$ if the LE lifetime is short (**Figure 3 of main text**)
- the sharp drop in $\Delta V_{OC,nr}$ for $\Delta E_{LE,CT} < 0.2\ eV$ producing a **universal sigmoidal function** valid for all measured blends. (**Figure 6 of main text**)

By showing that the LE ⇔ CT equilibrium fully explains the extensive dataset of this paper, we demonstrate that the following phenomena, previously considered important for maximizing EQE and $V_{OC,rad}$, play less important roles:

- The Marcus rate of exciton dissociation: in the presence of an equilibrium LE⇔ CT, the experimentally observed TRPL lifetime does not reflect the exciton dissociation rate but the removal of the LE ⇔ CT equilibrium by charge separation. Assuming typical electronic parameters for donor-acceptor systems, Marcus rates cannot explain exciton lifetimes in the hundreds of picosecond range (see Supplementary Figure 38).
- Hybridization of CT states with LE states is doubtlessly present, but the concomitant increase of radiative CT decay is not the reason for the sharp drop in $\Delta V_{OC,nr}$ for $\Delta E_{LE,CT} < 0.2\ eV$. Our analytical treatment shows that this drop is caused by the higher radiative quantum efficiency of LE states compared to CT states, the former becoming main actors for relaxation if the equilibrium shifts on the side of LE for vanishing driving forces.

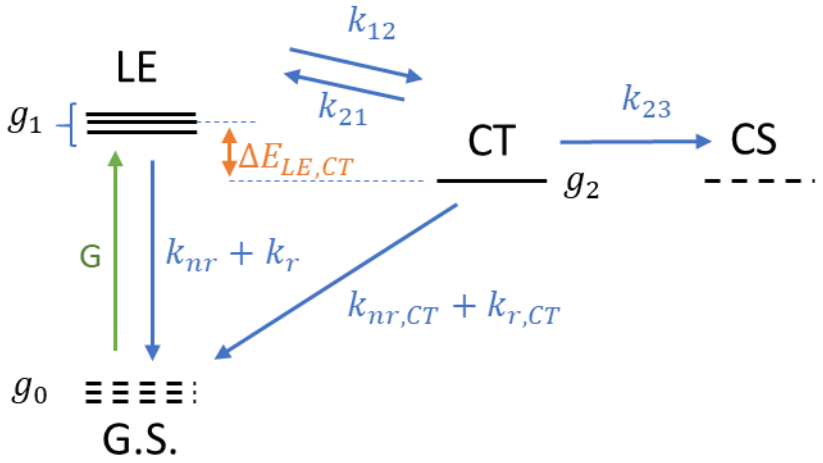

Supplementary Figure 24 | Kinetic model of the effective two-states model. States are given by black lines of different degeneracies (g_1, g_2). Dashed black lines are states that are not

included into the rate equation system. Blue arrows are first-order reactions with associated rate constants; green arrow indicated generation of LE states.

Our kinetic model is similar to the one in ref.[3] However, we do not take into account an equilibrium between charge separated (CS) and charge transfer (CT) states. We consider essentially an effective two-states model in which charge separation is considered as one additional lossy process acting on CT states (k_{23}, see Supplementary Figure 24). The equilibrium between LE and CT states is given by the forward and backward reactions k_{12} and k_{21}, respectively.
The relative occupation of LE and CT states, according to the Boltzmann probability distribution, is

$$p_{LE} = \frac{g_1}{Q} \cdot exp\left(-\frac{E_{LE}}{k_B T}\right);\ p_{CT} = \frac{g_2}{Q} \cdot exp\left(-\frac{E_{CT}}{k_B T}\right), \tag{4}$$

where E_{LE} and E_{CT} are the energies of the LE and CT states, respectively, $k_B = 8.617 \cdot 10^{-5}$ eV/K is the Boltzmann constant, T = 293 K is the temperature, and Q is the canonical partition function. The degeneracies g_1 and g_2 refer to the different densities of states in the bulk (for LE states) and at the interface (CT states), respectively. For bulk heterojunctions, one expects degeneracy ratios $g_{21} \equiv g_2/g_1 \approx 0.1$.[5] This yields for the equilibrium constant

$$K = \frac{p_{CT}}{p_{LE}} = g_{21} \cdot exp\left(\Delta E_{LE,CT}/k_B T\right), \tag{5}$$

where $\Delta E_{LE,CT} = E_{LE} - E_{CT}$. By solving the simple rate equation scheme for a reaction LE ⇔ CT for the stationary state, one can easily verify that

$$K = k_{12}/k_{21} \tag{6}$$

and therefore

$$k_{21} = \frac{k_{12}}{K} = \frac{k_{12}}{g_{21}} \cdot exp\left(-\frac{\Delta E_{LE,CT}}{k_B T}\right) = \frac{k_{12}}{g_{21} \cdot B}, \text{ where } B = exp\left(\frac{\Delta E_{LE,CT}}{k_B T}\right). \tag{7}$$

The system of ordinary differential equations corresponding to the kinetic scheme in Supplementary Figure 24 is given by the matrix equation

$$\dot{\boldsymbol{Y}} = \boldsymbol{T} \cdot \boldsymbol{Y} + \boldsymbol{G}, \tag{8}$$

where

$$\boldsymbol{Y} = \begin{bmatrix} LE \\ CT \end{bmatrix},\ \dot{\boldsymbol{Y}} = \frac{d\boldsymbol{Y}}{dt},\ \boldsymbol{T} = \begin{bmatrix} -(k_r + k_{nr} + k_{12}) & k_{21} \\ k_{12} & -\left(k_{r,CT} + k_{nr,CT} + k_{21} + k_{23}\right) \end{bmatrix},\ \boldsymbol{G} = \begin{bmatrix} g_{LE} \\ g_{CT} \end{bmatrix}. \tag{9}$$

Herein, **Y** is the state vector, comprising LE and CT which are time-resolved concentrations of LE and CT states, respectively, **T** is the transfer matrix and **G** is the generation vector. In the rate constants, the suffices “r” and “nr” refer to radiative and non-radiative processes, respectively, of the LE states, while the suffices “r,CT” and “nr,CT” refer to those of the CT states.

a Calculation of $\Delta V_{OC,nr}$: Simulation of stationary electroluminescence

Electroluminescence (EL) is measured under constant injection of carriers that recombine creating CT states that equilibrate with LE states. Both CT and LE decay either radiatively or non-radiatively; the sum of both, relative to the number of injected carriers, is the EL quantum yield. We assume that the yield of CT states from injected carriers is unity, which means that we ignore a possible charge recombination via deep traps (Shockley-Read-Hall recombination).
Following these considerations, we set $\dot{\boldsymbol{Y}} = 0$, $g_{LE} = 0$, $k_{23} = 0$ in (Supplementary Equation 9). Diagonalizing **T** and solving the system of linear equations (e.g using a symbolic math tool such as ***sympy***), we obtain the stationary densities $\mathbf{Y}_{st}$:

$$LE_{st} = -g_{CT} \cdot \frac{k_{12}}{k_{12}^2 - (k_{12} + k_{nr} + k_r)\cdot(g_{21}\cdot k_{nr,CT}\cdot B + g_{21}\cdot k_{r,CT}\cdot B + k_{12})} ;$$
$$CT_{st} = -g_{CT} \cdot g_{21} \cdot (k_{12} + k_{nr} + k_r) \cdot \frac{B}{k_{12}^2 - (k_{12} + k_{nr} + k_r)\cdot(g_{21}\cdot k_{nr,CT}\cdot B + g_{21}\cdot k_{r,CT}\cdot B + k_{12})} . \quad (10)$$

From the stationary concentrations under constant generation g_{CT}, we obtain the yields for emission from LE and CT (LEQY and CTQY, respectively) by comparing the respective pathways (k_r, $k_{r,CT}$, respectively) with the generation g_{CT}:

$$LEQY = LE_{st} \cdot \frac{k_r}{g_{CT}}; CTQY = CT_{st} \cdot \frac{k_{r,CT}}{g_{CT}} \quad . \quad (11)$$

Combining (Supplementary Equation 11) with (Supplementary Equation 10), we find for the total internal emission quantum yield:

$$ELQY_{int} = LEQY + CTQY$$
$$= -\frac{g_{21} \cdot k_{r,CT} \cdot (k_{12} + k_{nr} + k_r) \cdot B + k_{12} \cdot k_r}{k_{12}^2 - (k_{12} + k_{nr} + k_r) \cdot (g_{21} \cdot k_{nr,CT} \cdot B + g_{21} \cdot k_{r,CT} \cdot B + k_{12})} \quad (12)$$

The total internal emission quantum yield can be related to the non-radiative V_{OC} loss by[6]:

$$\Delta V_{OC,nr} = -k_B T \cdot ln(ELQY_{ext}), \quad (13)$$

where the external electroluminescence quantum yield is given by

$$ELQY_{ext} = ELQY_{int} \cdot p_e;\ p_e < 1. \quad (14)$$

In Supplementary Figure 25a, we plot (Supplementary Equation 13) varying $\Delta E_{LE,CT}$ from +0.3 to -0.1 eV, fixing all other parameters to the following values: k_{12}=1e11 s^{-1}, $k_r = 1.9 \cdot 10^6$ s^{-1}, $k_{nr}=1.9 \cdot 10^9$ s^{-1}, $k_{rct}=1.9 \cdot 10^4$ s^{-1}, $k_{nrct}=1.9 \cdot 10^9$ s^{-1}, $k_BT=8.617 \cdot 10^5$ *293 eV, pe=0.3, g_{21}=0.1. In panel a, we vary k_{12} between 10^9 and 10^{13} s-1, showing that Marcus rates do not influence the functional shape significantly as long as they are above 10^{10} s^{-1}, a condition that can be considered as safe for donor-acceptor bulk heterojunctions (see Supplementary Figure 38). The curves in Supplementary Figure 25a clearly show three regimes: a plateau for $\Delta E_{LE,CT} > 0.2\ eV$ where the non-radiative voltage losses are controlled exclusively by the CT state, another plateau for

$\Delta E_{LE,CT} < 0\ eV$ where they are controlled by the LE state, and a sigmoidal regime where both LE and CT contribute to the nonradiative voltage losses according to the Boltzmann equilibrium.

To further investigate the parameter dependencies of this analytical model, we varied all fitting parameters over several orders of magnitude. In panel b, we vary the degeneracy ratio g_{12} from 0.001 to 1, showing that a lower ratio of CT/LE states shifts the curve to the right. In Supplementary Figure 25c, we have applied a factor f_{ct} to both k_{nrct} and k_{rct}, to show that the total CT decay rate influences the inflection point of the curves but not the maximum, which is controlled by the ratio k_{rct}/k_{nrct}. Thus, we find that both g_{12} and f_{ct} act on the position of the inflection point and therefore exhibit a linear dependency. Fitting the correct position of the inflection point in the experimental data can thus be achieved by tuning f_{ct} or g_{12}. Effectively, a relatively small value for g_{12} requires a larger value for f_{ct}, while in contrast a relatively small value for f_{ct} requires a larger value for g_{12}, causing large uncertainties. Ultimately this means that g_{12} and f_{ct} cannot be fitted simultaneously, but one of these values should ideally be determined by other methods. To fit the experimental $\Delta V_{OC,non\text{-}rad}$ data, we thus fix the degeneracy ratio to the previously reported typical value for OSCs, $g_{12} = 0.1$.

To obtain a more thorough understanding of the sigmoidal shape for $\Delta V_{OC,non\text{-}rad}$, we investigated the influence of temperature. In Supplementary Figure 25d, we show that decreasing temperature, the step height gets smaller and the equilibrium range gets narrower. However, the maximum slope is independent of temperature, as shown by representing the first derivatives in Supplementary Figure 25e. It is found that while the derivatives get narrower with temperature, the maximum slope is always 0.8 V/eV for CTQY/LEQY = 0.01 ($\Delta V_{OC,non\text{-}rad}$ = 120 mV at 300K), which is a typical value for the systems investigated in this study. As shown further below, this maximum slope is indeed reached by our data, which is a further confirmation for the validity and dominance of the LE ⇔ CT equilibrium for nonradiative voltage losses at negligible driving force in the investigated OSCs.

Finally, we investigated the influence of the CTQY/LEQY ratio. In Supplementary Figure 25f, we displaced the curves horizontally such that the inflection point occurs at zero, and we normalized the curves between zero and one. In such a representation, chosen also for Figure 6b in the main text, the curve form depends only on the temperature and weakly on the ratio of CTQY/LEQY so that for ratios in the same order of magnitude, a universal curve form is expected, independent of the precise values of the elementary rate constants for CT and LE decay. Hence, the fact that all our data follow this universal curve form within experimental error, is a strong argument that nonradiative voltage losses are controlled by the Boltzmann equilibrium, and that other factors, such as Marcus rates, morphology changes or hybridization, are of minor importance. Note that in the calculation of Supplementary Equation 13 the values for the radiative decay rate of the CT state, $k_{r,CT}$, have not been changed, which means that the effect of a higher oscillator strength of strongly hybridized CT states for smaller $\Delta E_{LE,CT}$ values has not been considered. Still, the agreement with all our donor-acceptor combinations is nearly perfect (see Supplementary Figure 28).This fact is a strong evidence that the sharp drop of $\Delta V_{OC,nr}$ for $\Delta E_{LE,CT} < 0.2\ eV$ is entirely due to an equilibrium LE ⇔ CT. At vanishing driving forces, the main actor for radiative and non-radiative recombination becomes the LE state, while the CT state becomes less relevant.

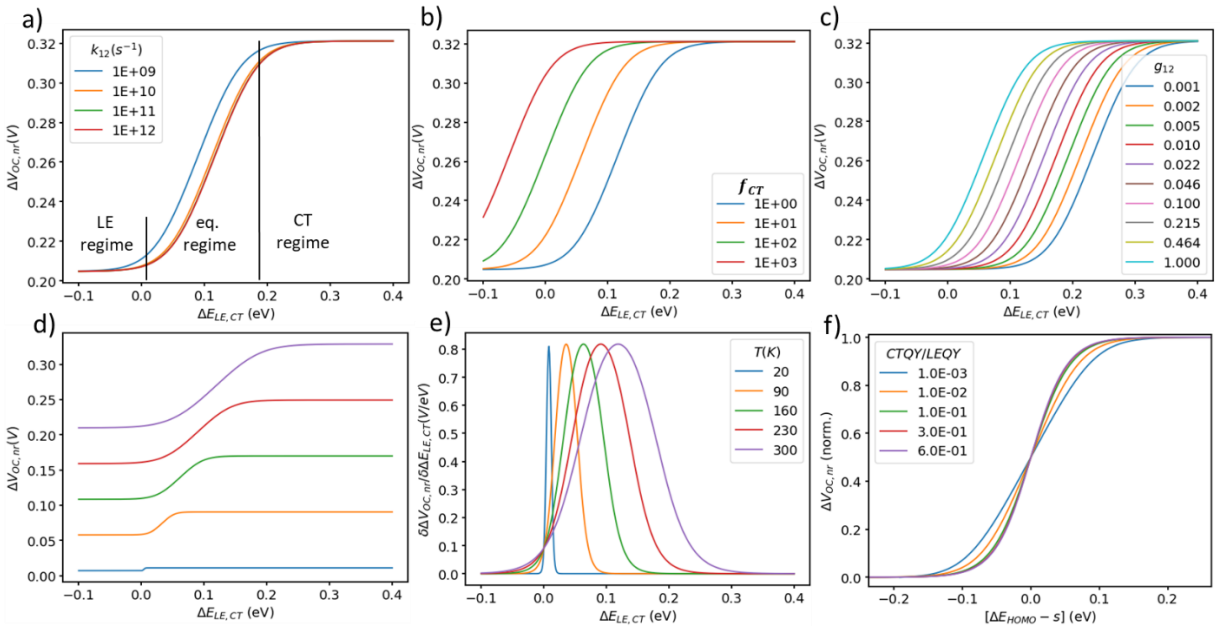

Supplementary Figure 25 | In-depth modeling of $\Delta V_{OC,non\text{-}rad}$ by variation of parameters. a) Calculation of $\Delta V_{OC,non\text{-}rad}$ from Supplementary Equation 13, varying the exciton splitting rate constant k_{12}, **b)** varying the degeneracy ratio g_{21} with logarithmic step width, **c)** applying a factor f_{ct} to both k_{rct} and k_{nrct} , **d)** varying the temperature T as given in the inset of panel **e)**. **e)** first derivatives of the curves in panel **d)**, showing that the maximum slope is independent of temperature and characteristic for a given ratio of CTQY/LEQY, here assumed 10^{-2}, typical for our samples. **f)** horizontally displaced and normalized curves for different ratios of the PL quantum yields of CT and LE states.

b) Calculation of IQE: simulation of constant photoexcitation

For the simulation of photovoltaic performance, we set $\dot{Y} = 0$ and $g_{CT} = 0$, thus ignoring the small contribution to the creation of photoexcited states via a possible hybridization of CT and LE states. Given the lower density of states of CT states at the interface, this will lead to only a very small error.

From Supplementary Equation 9, we obtain the stationary densities $\mathbf{Y}_{st}$:

$$LE_{st} = -g_{LE} \cdot \frac{g_{21} \cdot k_{23} \cdot B + g_{21} \cdot k_{nr,CT} \cdot B + g_{21} \cdot k_{r,CT} \cdot B + k_{12}}{k_{12}^2 - (k_{12} + k_{nr} + k_r) \cdot (g_{21} \cdot k_{23} \cdot B + g_{21} \cdot k_{nr,CT} \cdot B + g_{21} \cdot k_{r,CT} \cdot B + k_{12})}$$

$$CT_{st} = -g_{LE} \cdot g_{21} \cdot k_{12} \cdot \frac{B}{k_{12}^2 - (k_{12} + k_{nr} + k_r) \cdot (g_{21} \cdot k_{23} \cdot B + g_{21} \cdot k_{nr,CT} \cdot B + g_{21} \cdot k_{r,CT} \cdot B + k_{12})} \quad (15)$$

Ignoring charge recombination (extraction losses), we can associate the internal quantum yield with the charge separation yield:

$$IQE = CT_{st} \cdot \frac{k_{23}}{g_{LE}} \tag{16}$$

Ignoring extraction losses is justified by the fact that the experimental data in Figure 3 of the main text show that the reduction of EQE can be dominantly ascribed to charge separation losses. Inserting Supplementary Equation 16 into Supplementary Equation 15, we obtain

$$IQE = -g_{21} \cdot k_{12} \cdot k_{23} \cdot \frac{B}{k_{12}^2 - (k_{12} + k_{nr} + k_r) \cdot \left(g_{21} \cdot k_{23} \cdot B + g_{21} \cdot k_{nr,CT} \cdot B + g_{21} \cdot k_{r,CT} \cdot B + k_{12}\right)} \tag{17}$$

In Supplementary Figure 26a we plot Supplementary Equation 17 varying $\Delta E_{LE,CT}$ from +0.3 to -0.1 eV in linear steps, and $\tau_{nr} = 1/k_{nr}$ from 100 ps to 10 ns in logarithmic steps, fixing all other parameters to the following values: k_{12}=1e11 s^{-1}, k_{23}=5e10 s-1, k_r=1.9e6 s^{-1}, k_{rct}=1.9e4 s^{-1}, k_{nrct}=1.9e9 s^{-1}, k_BT=8.617e-5*293 eV, pe=0.3, g_{21}=0.1.

Supplementary Figure 26b shows a striking agreement with the measured data. It immediately evidences a ***central design principle*** for systems with low diving force for exciton dissociation: even if the driving force is effectively zero, we can still get more than 90% IQE if the lower bandgap component has a singlet lifetime of a few nanoseconds. If the singlet lifetime is below 1 ns, then IQE collapses. Note that we have not varied k_{12} nor k_{23} in the production of Supplementary Figure 26b. This shows that the reason for the slower charge separation at vanishing driving forces is not slower exciton breaking, as might be expected from Marcus theory, but slower charge separation due to the fact that the only species that can be converted into CS state, namely CT states, are present in very low concentrations if the equilibrium is strongly on the LE side. We give a simple analytical treatment of this fact in the next section.

To further investigate the parameter dependencies and of this analytic model regarding IQE, we varied all fitting parameters over several orders of magnitude. In Supplementary Figure 26c, we have applied a factor f_{ct} to both k_{nrct} and k_{rct}, to show that the total CT decay rate dominantly influences maximum IQE while the inflection point shows only a minor dependency. In contrast, varying the degeneracy factor g_{12} influences only the inflection point but not the maximum IQE, see Supplementary Figure 26d. Variation of the charge separation constant k_{23} influences both the inflection point and the maximum IQE, see Supplementary Figure 26e. In summation, the parameters g_{12}, k_{23}, and f_{ct} are interdependent and similar IQE curves can be obtained by different parameter combinations, which also causes large uncertainties in the fit parameters. In accordance with fitting of $\Delta V_{OC,non\text{-}rad}$, g_{12} is thus fixed to a value of 0.1.

Finally, we investigate the influence of the rate of exciton dissociation on the IQE. In Supplementary Figure 26f, the exciton splitting rate constant k_{12} is varied over several orders of magnitude. As long as $k_{12} > 10^{11}$ s^{-1}, which can be considered as a safe condition (Supplementary Figure 38), IQE is independent of k_{12}.

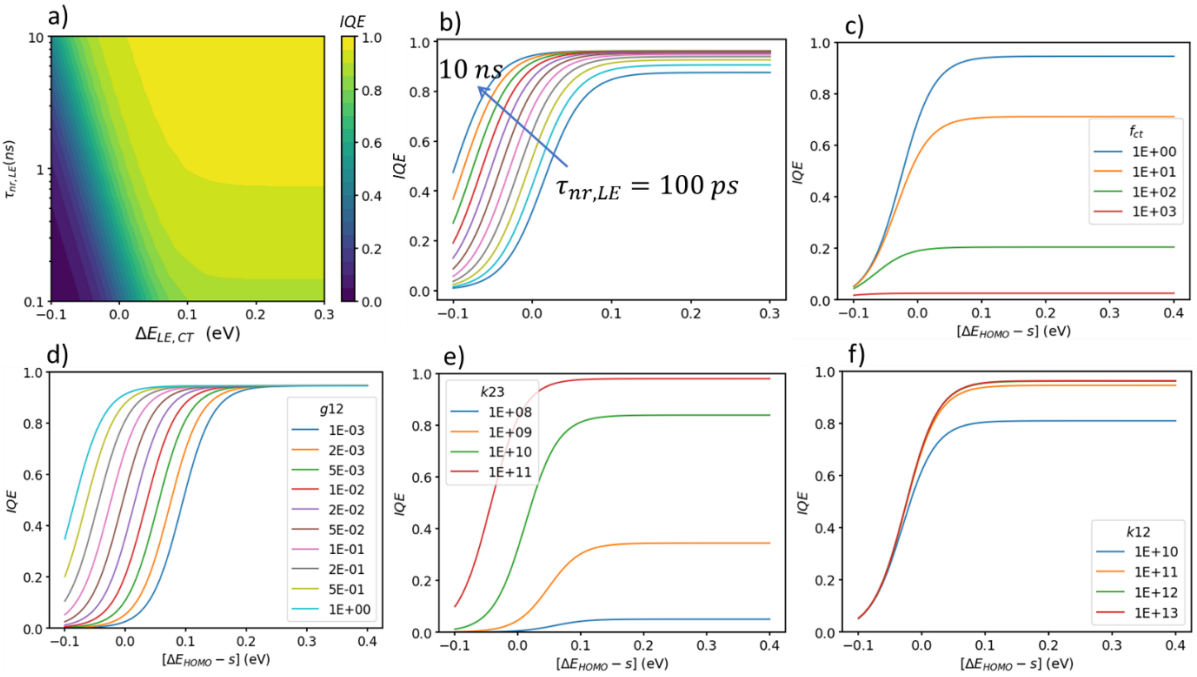

Supplementary Figure 26 | In-depth analysis of IQE by varying all parameters. a) In a two-dimensional false color representation showing the impact of non-radiative lifetime of LE states.**b)** The same is in **a)** but in a parametric representation. **c)** Applying a factor f_{ct} to both k_{nrct} and k_{rct}. **d)** Varying the degeneracy ratio g_{12}. **e)** Varying the charge separation constant k_{23} **f)** Variation of the exciton splitting rate constant k_{12};

c) Influence of $\Delta E_{LE,CT}$ on the total LE deactivation time

The different curves in Supplementary Figure 26b have been calculated for different values of $\tau_{nr} = 1/k_{nr}$. However, in each single curve, the value for all "lossy" rate constants (k_r, k_{nr}, k_{rct}, k_{nrct}, k_{23}) was kept constant. Only $\Delta E_{LE,CT}$ and thus the position of the LE⇔CT equilibrium was changed. Obviously, the equilibrium position has a strong influence on IQE, which can only mean that the equilibrium position has a strong influence on the rate at which excitons are converted into charge separated states.

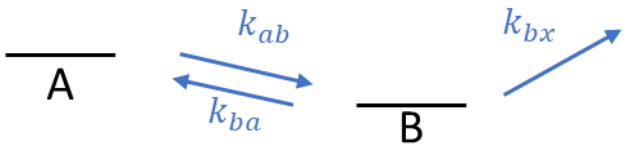

Supplementary Figure 27 | Simplified kinetic model. This model is applied to understand the influence of the equilibriumposition on the deactivation rate of the partner that is not quenched

Consider a simple equilibrium A⇔B with just one lossy process k_{bx} acting on B only (see Supplementary Figure 27). If $k_{bx} \ll \{k_{ab}, k_{ba}\}$, then the lossy process will not disturb the equilibrium position significantly:

$$\frac{B_{st}}{A_{st}} \approx \frac{k_{ab}}{k_{ba}} = K. \quad (18)$$

Starting from the stationary state, the rate of the lossy process is

$$R = B_{st} \cdot k_{bx} \quad (19)$$

However, as we assumed that equilibration is much faster than quenching by the lossy process, B will be constantly replenished by the equilibrium. Therefore, the total rate of disappearance of (A+B=C) is given by:

$$\frac{d(C)}{dt} = R; \text{ C=A+B} \quad (20)$$

Inserting Supplementary Equation 20 into Supplementary Equation 18:

$$K \approx \frac{B_{st}}{A_{st}} = \frac{B_{st}}{(C_{st} - B_{st})}; \quad (21)$$

and solving for B_{st},

$$B_{st} \approx K \cdot \frac{C_{st}}{(1+K)} \quad . \quad (22)$$

Finally inserting Supplementary Equation 22 into Supplementary Equation 19,

$$\frac{dC_{st}}{dt} \approx K \cdot \frac{C_{st}}{(1+K)} \cdot k_{bx} \quad . \quad (23)$$

The lifetime of the total equilibrium is thus:

$$\tau_{tot} = \frac{1+K}{K \cdot k_{bx}}. \quad (24)$$

Supplementary Equation 24 shows that the experimentally observed increase of exciton lifetimes for systems with small driving force can be **entirely explained by shifting of the equilibrium to the LE side**: Only if $K \to \infty$, that is, if the equilibrium is fully on the B side, then $\tau_{tot} \approx \frac{1}{k_{bx}}$. As soon as the equilibrium shifts towards A, τ_{tot} increases. In conclusion, we find that it is not the exciton splitting rate that increases the exciton lifetime for low driving forces, but the lower amount of CT states in the dynamic equilibrium, slowing down charge separation.

d) Fitting to actual dataset

In order to apply the fitting functions in Supplementary Equations 13 and 17 to model our dataset, we must consider that the IQE data in Figure 3 and the $\Delta V_{OC,nr}$ data in Figure 6 of the main paper, are not given as function of $\Delta E_{\mathrm{LE},CT}$ but as function of $\Delta HOMO$. The difference between these energies is equivalent to the difference in energy of a CT state and a fully charge separated state, which we denote as χ. This parameter shifts the fitted curves horizontally and has therefore the same effect as the degeneracy factor g_{21}, see Supplementary Figure 25b, or f_{ct}, see Supplementary Figure 25c. In principle, χ could be obtained by measuring the energy of the CT state. However it has been shown recently that CT emission stems from non-equilibrium CT states and does not refer to CT equilibrium states.[7] Moreover, at very low driving forces, which are the focus of the present paper, the occurrence of hybridization severely hampers the

determination of the CT state energies. For this reason, we fix $\chi = 0.03eV$. If the actual value for χ becomes available, the fitted values for f_{ct} (as g_{12} is fixed to 0.1) can be adapted accordingly.

From this it follows that fitting the curves in Supplementary Figure 25 to actual datasets involves adjustments of k_{rct}, k_{nrct}, and as these will differ among blends, while g_{12} is fixed to 0.1 due to the functional dependencies. The curves in Supplementary Figure 26 will additionally depend on k_{23}. It is therefore possible to perform a multi-objective optimization to fit both the experimental datasets, $IQE = f(\Delta HOMO)$ and $\Delta V_{OC,nr} = f(\Delta HOMO)$, with the same model and the same set of parameters.

Using this fitting strategy, we found close to perfect fits of Supplementary Equation 13 to the experimental non-radiative voltage losses (Supplementary Figure 28), and we found good fits of Supplementary Equation 17 to the experimental IQE values, see Supplementary Figure 29a. It can be noted that for those acceptors which show a drop of IQE at low driving forces (o-IDTBR and eh-IDTBR, green and purple curves, respectively), the maximum achievable IQE values for high driving forces are not rendered correctly. Considering charge recombination in an effective three-state model, both the rising part and the maximum IQE values are rendered correctly. This means that our effective two-state model renders well both non-radiative voltage losses and IQE at low driving forces, while at high driving forces, the influence of the CS⇔CT equilibrium should be taken into account.

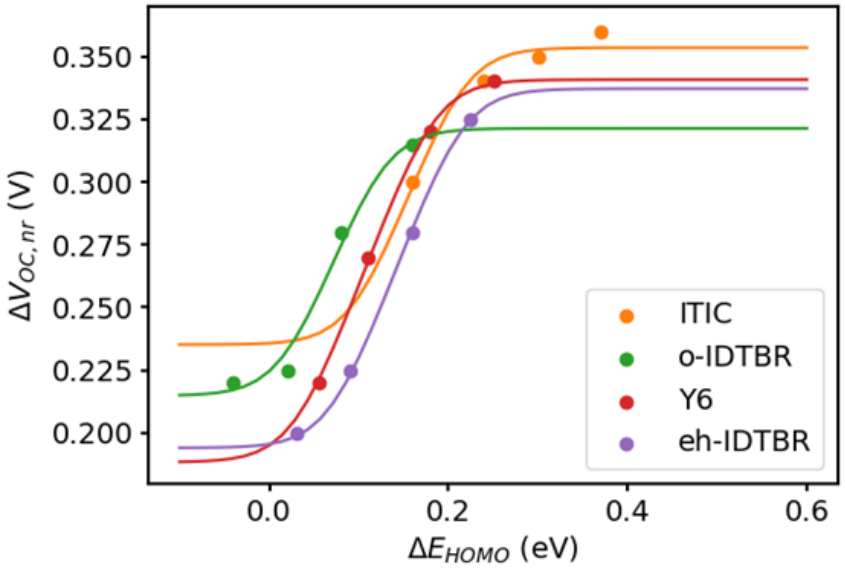

Supplementary Figure 28 | Fit of $\Delta V_{OC,non\text{-}rad}$. Fit of all blends to Supplementary Equation 13, using the parameters in Supplementary Table 4.

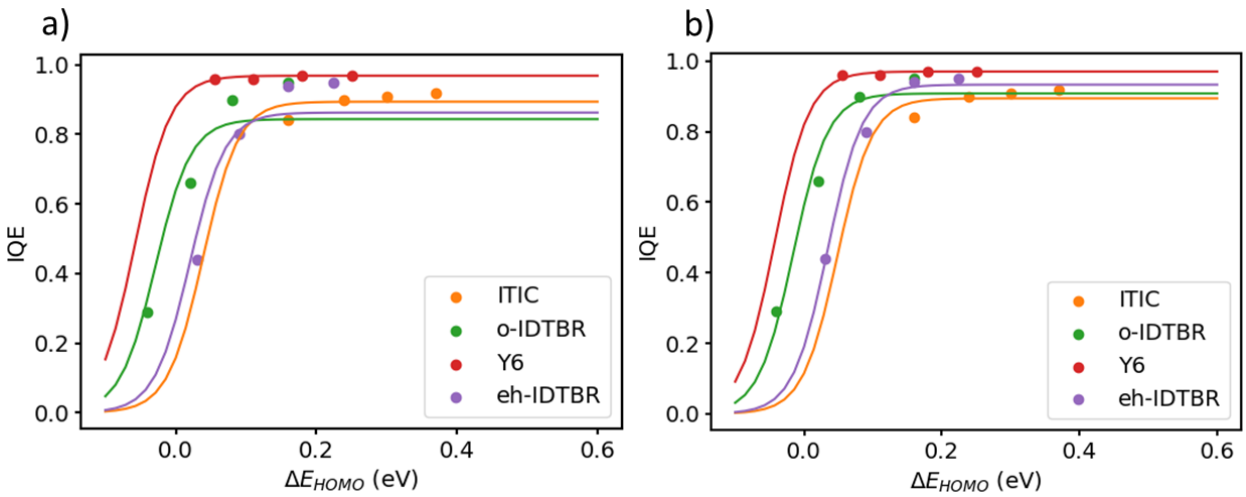

Supplementary Figure 29 | Fits of IQE. a) Fit of all blends to Supplementary Equation 17, using the parameters in Supplementary Table 4. Fits obtained by a multi-objective optimization, fitting Supplementary Equations 13 and 17 at the same time with the same set of parameters as given in Supplementary Table 4; b) Fits obtained by a multi-objective optimization explicitly considering charge recombination from CS to CT in the scheme in Supplementary Figure 24, with the parameter set given in Supplementary Table S5. Charge separated states were assumed 0.03 eV lower in energy with a degeneracy ratio g(CS)/g(CT)=30. An extraction rate constant k_{ext}=2e8 was assumed acting on CS states.

Supplementary Table 4: Fitting parameters for the fits in Supplementary Figures 28 and 29a, using an effective two state model. Uncertainties (square roots of self-covariances) in brackets.

Acceptor	k_r [s^{-1}] (fixed)	$k_{r,ct}$ [s^{-1}]	$k_{nr,ct}$ [s^{-1}]	g_{21}(fixed)	k_{23} [s^{-1}]
ITIC	1.0e5	7(1)e3	2.4(5)e9	0.1	2(1)e10
o-IDTBR	1.2e6	3(1)e5	2.8(6)e10	0.1	1.5(9)e11
Y6	1.9e6	4.5(4)e4	9.8(5)e9	0.1	3(3)e11
eh-IDTBR	1.7e6	1.2(2)e4	2.2(2)e9	0.1	1.4(3)e10

Supplementary Table 5: Fitting parameters for the fits in Supplementary Figures 28 and 29b, using an effective three state model explicitly considering recombination for the calculation of IQE. Due to the high number of parameters, uncertainties are always higher than 200%, in some cases even 1000%, so that different combinations of parameters might give a similarly good fit. This table and the corresponding Supplementary Figure 29b merely serve as a demonstration that the IQE fit quality can be improved if charge recombination is considered.

Acceptor	k_r [s^{-1}]	$k_{r,ct}$ [s^{-1}]	$k_{nr,ct}$ [s^{-1}]	g_{21}	k_{23} [s^{-1}]
ITIC	1.0e5	4e3	8e8	0.15	2e10
o-IDTBR	1.2e6	1.2e4	5e8	1.73	8e9
Y6	1.9e6	6e3	4e8	0.88	4e12
eh-IDTBR	1.7e6	9e3	2e8	0.21	5e9

In Supplementary Figure 30 and 31, we have chosen two special representations of the data and fits of Supplementary Figure 28 to further demonstrate that the Boltzmann equilibrium between LE and CT states governs non-radiative voltage losses. In Supplementary Figure 30, we have horizontally displaced all curves such that the inflection point is at zero energy, and we normalized the y axis between zero and one. As we have shown in Supplementary Figure 25f, such a representation yields quasi identical spectral shapes, irrespective of the values for the individual CT and LE decay constants, as long as the ratio CTQY/LEQY is similar for all curves. Supplementary Figure 30 shows that all experimental data points follow this universal curve shape. Even the behavior of o-IDTBR (green symbols) is fully in agreement with the predictions from Supplementary Figure 25f, which predicts that the normalized slope is slightly steeper if the ratio CTQT/ELQY is closer to one. Indeed, o-IDTBR shows only a dynamics of about 100 mV in Supplementary Figure 28, which is less than the other samples, showing typically a dynamics of 120-150 meV, which at 300K is equivalent to about two orders of magnitude of difference between LEQY and CTQY.

Supplementary Figure 31 is similar to Supplementary Figure 30, but the curves are not normalized. A blue dashed line is given with a slope of 0.8 V/eV, expected if the ratio CTQY/LEQY = 0.01, see Supplementary Figure 25f. We find that most of our acceptors show this maximum slope in the inflection point except o-IDTBR of which we know that its ratio CTQY/LEQY > 0.01, and therefore a smaller maximum slope is expected.

In conclusion, we find that our full dataset reproduces even the predicted details of the equilibrium model, which means that a Boltzmann equilibrium is largely responsible for the nonradiative voltage losses.

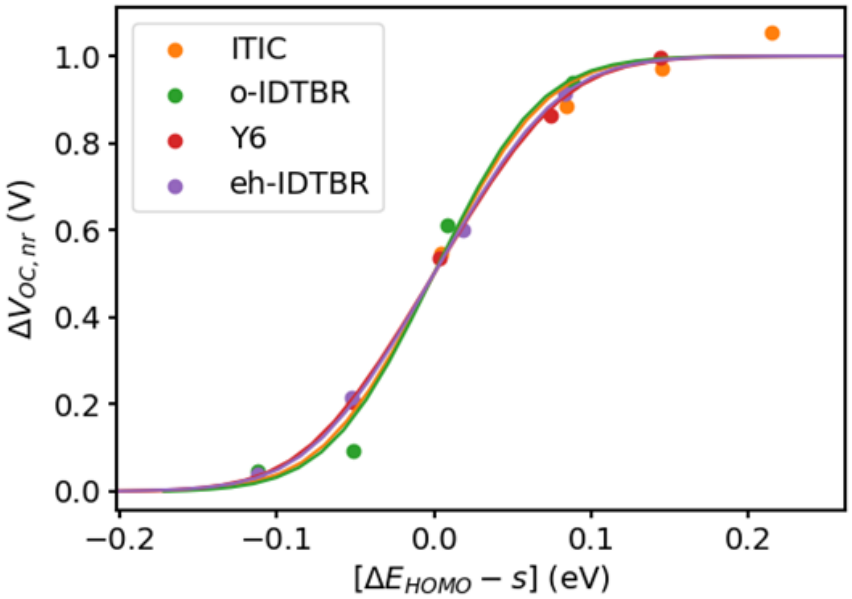

Supplementary Figure 30 | Dependence of the normalized nonradiative voltage loss on the effective energy offset $\Delta E_{LE,CT} - s$. Here s is the inflection point of the corresponding fitted function in Supplementary Figure 28. The slope of all datasets is the same and depends only on temperature, thus showing that nonradiative voltage losses at low driving forces are essentially controlled by the Boltzmann equilibrium between LE and CT.

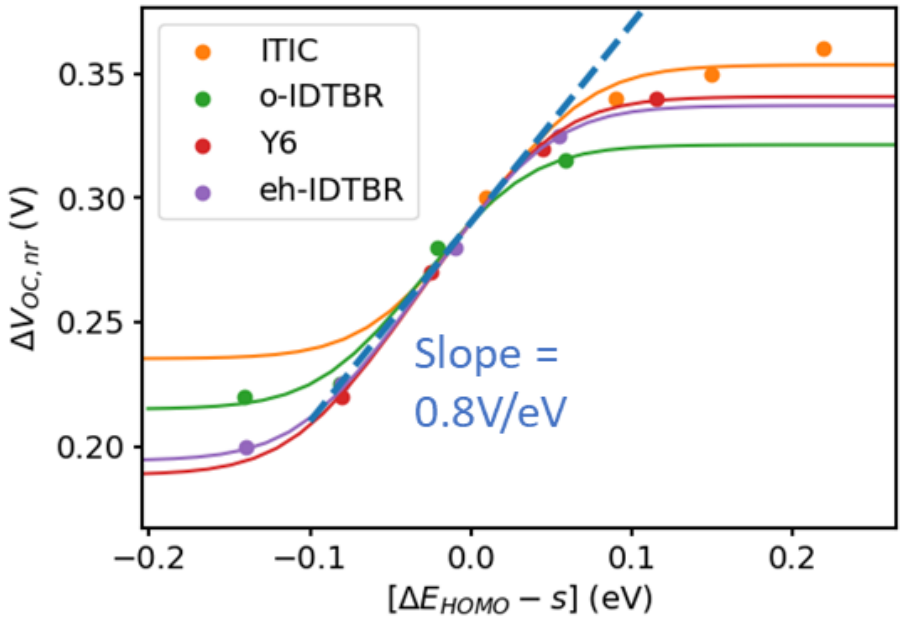

Supplementary Figure 31 | Intersystem comparison of $\Delta V_{OC,non\text{-}rad}$ for shifted ΔE_{HOMO}. The same data as in Supplementary Figure 28, but all curves displaced horizontally (but not vertically) to intersect at $\Delta V_{OC,non-rad} = 0.29$ V. The dashed blue line has a slope of 0.8 V/eV, which is expected for a Boltzmann equilibrium if the ratio CTQY/LEQY is about 0.01.

Supplementary Note 3: Ground state absorption and photoluminescence spectra

The TRPL transients in the main text (Figure 3) have been performed without wavelength selectivity on the detection side. As shown in Supplementary Figures 32 – 35 below (dashed lines), at the pumping energy of 3.1 eV, both donor and acceptor show significant ground state absorption (GA). Nonetheless, the steady-state photoluminescence (PL) spectra of the blends generally match very closely the PL spectra of the pure acceptor films, compare green and orange solid curves, respectively (and Supplementary Figures 36 and 37). The absence of donor PL in the composite PL spectrum of the blend can be explained by ultrafast breaking of the higher energetic donor exciton, which is expected to be a non-equilibrium process which in some cases has been shown to be even faster than predicted for Marcus theory which is valid for thermodynamic equilibrium.[8]
However, some of our blends do show some small residual contribution of donor PL in the blend spectrum, see for example WF3S:Y6 in Supplementary Figure 33. Therefore, we quantified the spectral weight of the normalized donor and acceptor PL (B_D and B_A, respectively, where B stands for "basis vector") in the normalized PL spectrum S of the blend, assuming linear superposition:

$$\boldsymbol{S} = \boldsymbol{w} \cdot \boldsymbol{B} \tag{25}$$

Herein, **S** is a single row vector, the weight coefficients $w = \{w_d, w_a\}$ are arranged as a row vector, and **B** is a matrix containing B_d and B_a as row vectors. The weight coefficients are obtained by a Moore-Penrose pseudo matrix inversion according to

$$\boldsymbol{w} = \boldsymbol{S} \cdot \boldsymbol{B}^{-1} \tag{26}$$

From the weight coefficients, we calculate the relative donor contribution X(D) as

$$X(D, 488\,nm) = w_d/(w_d + w_a) \tag{27}$$

which are valid at the excitation wavelength of the PL spectra in Supplementary Figures 32 – 35, namely 488 nm (2.5 eV, see red vertical arrows). For the TRPL traces, excitation was done at 402 nm (3.1 eV, purple arrows). At this wavelength, relatively more acceptor absorption is found than at 488 nm, which is taken into account by linear scaling of X(D,488 nm) with the ratio of the GA spectra. The resulting estimated values for X(D, 402 nm) are given in the respective panels below. We find that in most cases, X(D,402 nm) is within a few percent range, while a maximum X(D, 402) of about 12.6 % is found for WF3:ITIC. However, even at this amount of donor PL, as specific evaluation of the exciton splitting lifetime of acceptor excitons should still be possible by our tri-exponential model function.

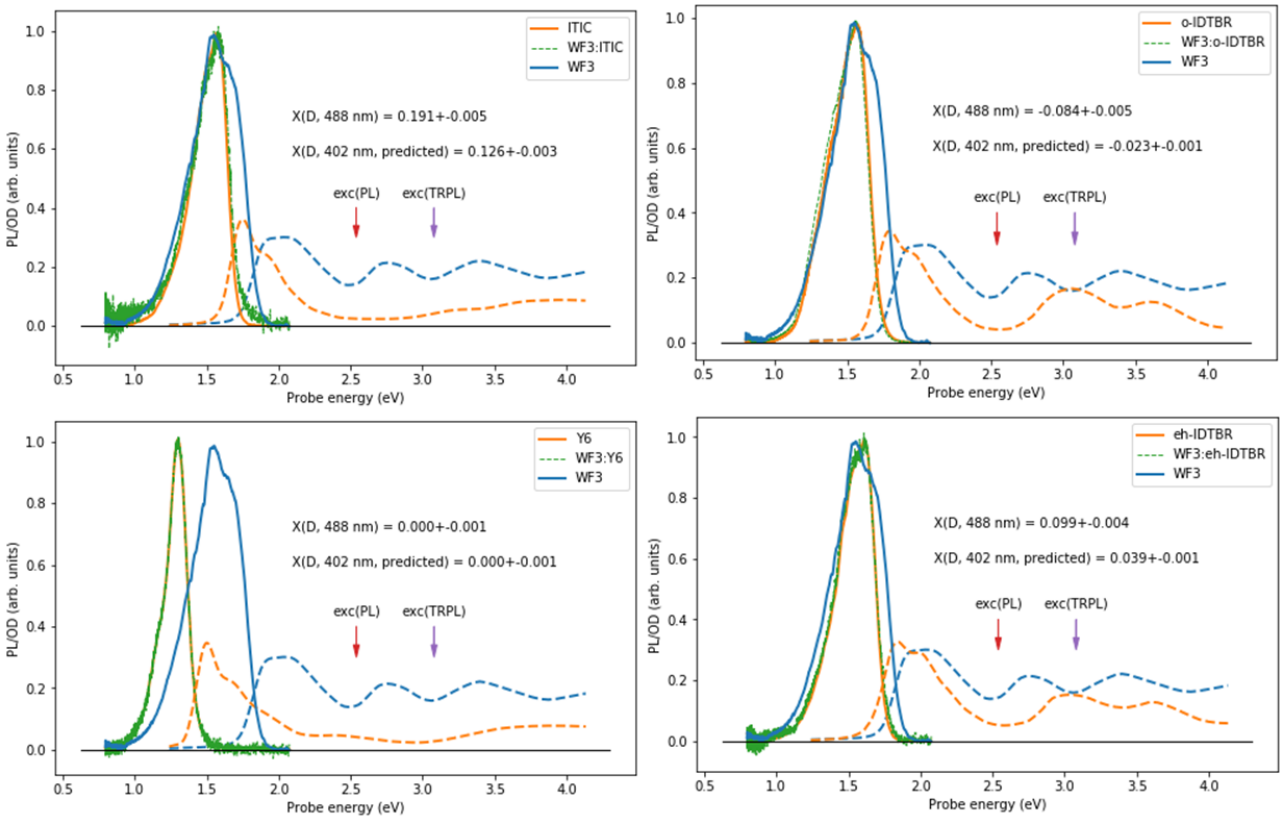

Supplementary Figure 32 | Analysis of PL contribution of polymer donor in WF3 solar cells. Ground state absorption (dashed) and PL (solid) spectra of a WF3 film (blue) and of solar cells consisting of a blend of the donor WF3 and one of the acceptors (green). The pure acceptor is given in orange. Vertical red and purple arrows indicate the pumping energies for the PL and the TRPL experiment, respectively.

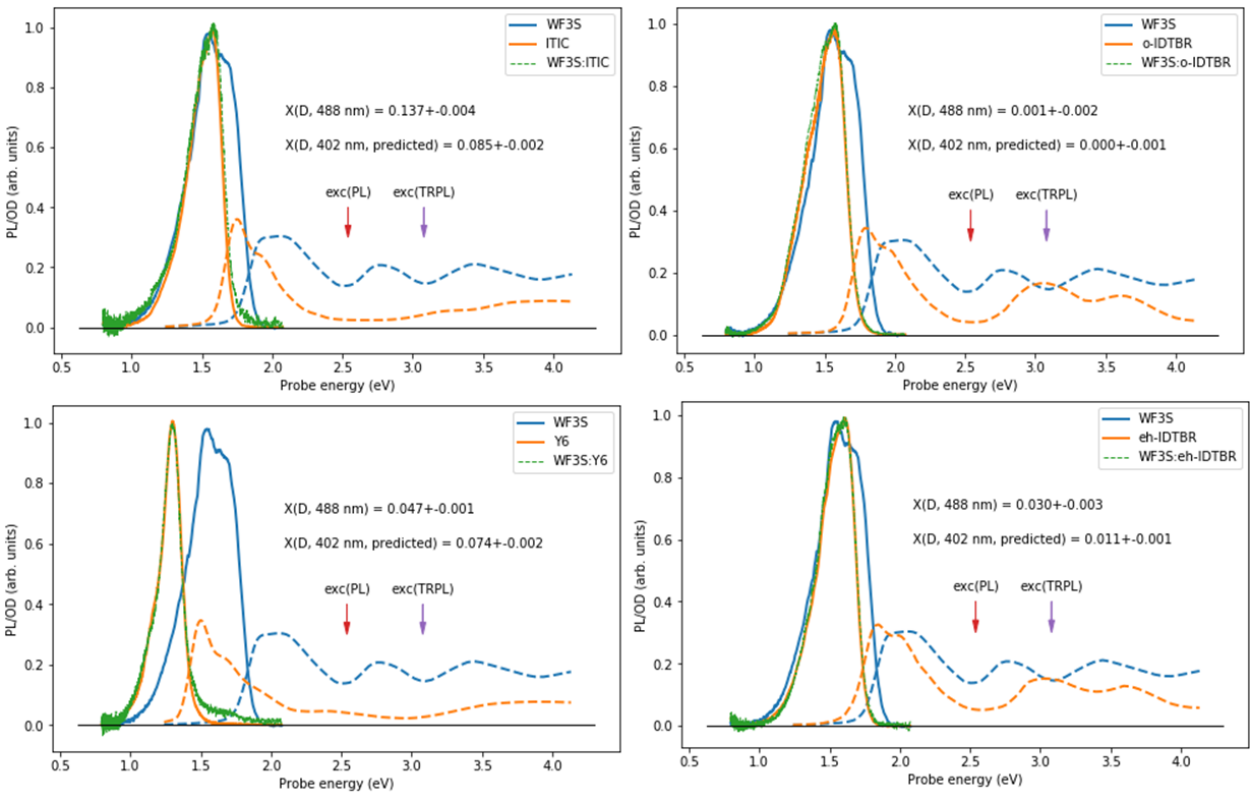

Supplementary Figure 33 | Analysis of PL contribution of polymer donor in WF3S solar cells. Ground state absorption (dashed) and PL (solid) spectra of a WF3S film (blue) and of solar cells consisting of a blend of the donor WF3S and one of the acceptors (green). The pure acceptor is given in orange. Vertical red and purple arrows indicate the pumping energies for the PL and the TRPL experiment, respectively.

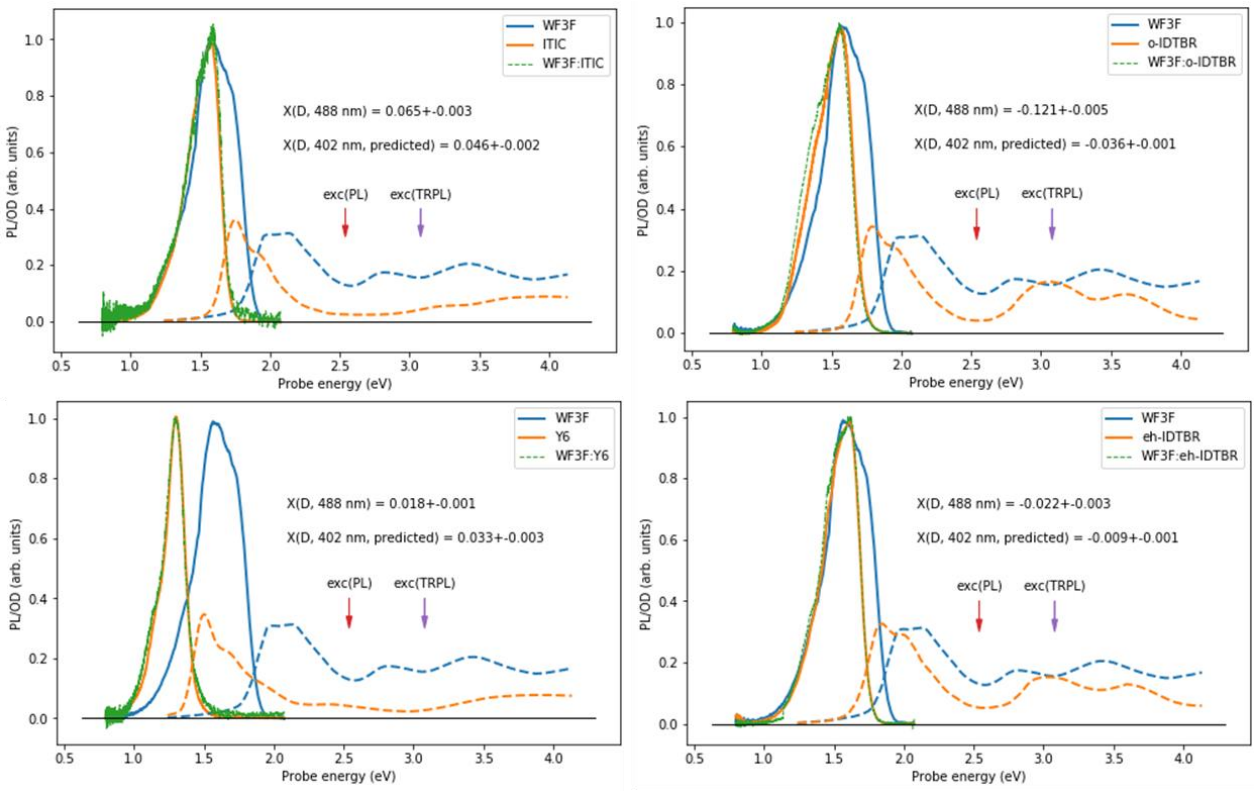

Supplementary Figure 34 | Analysis of PL contribution of polymer donor in WF3F solar cells. Ground state absorption (dashed) and PL (solid) spectra of a WF3F film (blue) and of solar cells consisting of a blend of the donor WF3F and one of the acceptors (green). The pure acceptor is given in orange. Vertical red and purple arrows indicate the pumping energies for the PL and the TRPL experiment, respectively.

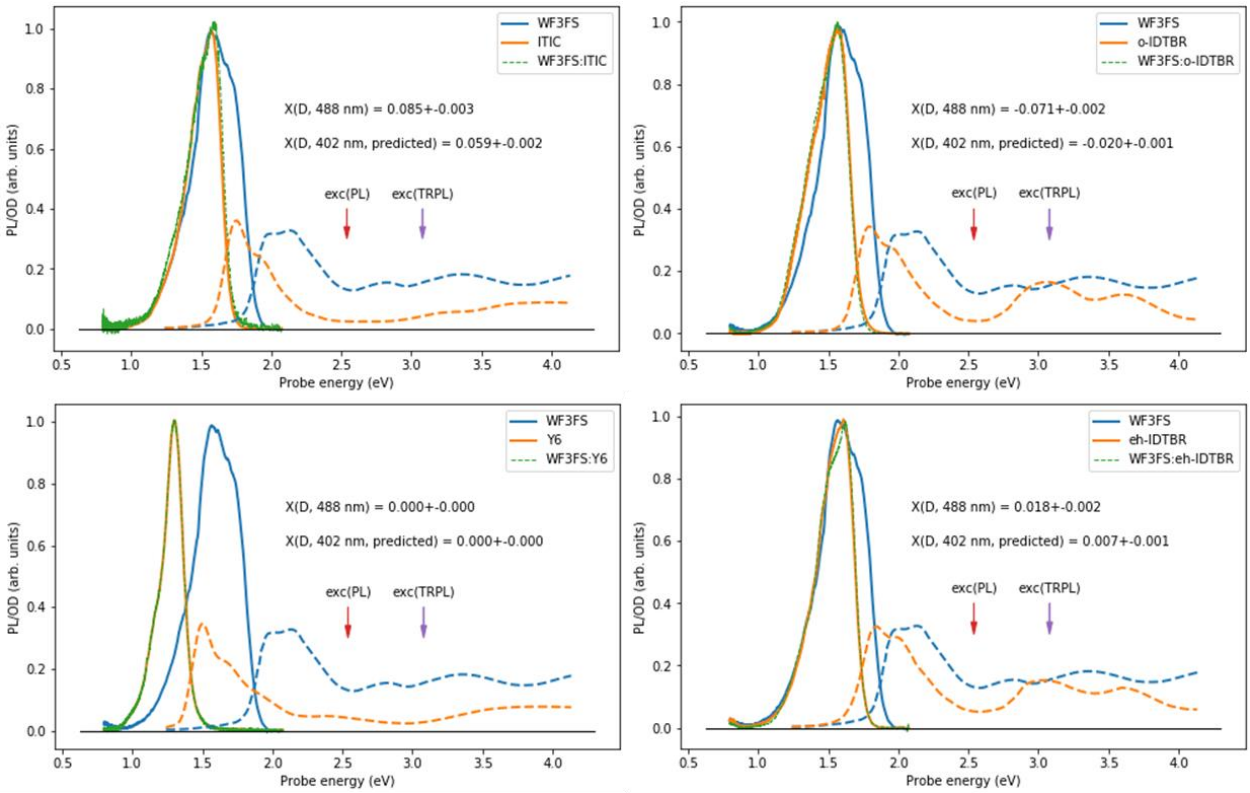

Supplementary Figure 35 | Analysis of PL contribution of polymer donor in WF3FS solar cells. Ground state absorption (dashed) and PL (solid) spectra of a WF3FS film (blue) and of solar cells consisting of a blend of the donor WF3FS and one of the acceptors (green). The pure acceptor is given in orange. Vertical red and purple arrows indicate the pumping energies for the PL and the TRPL experiment, respectively.

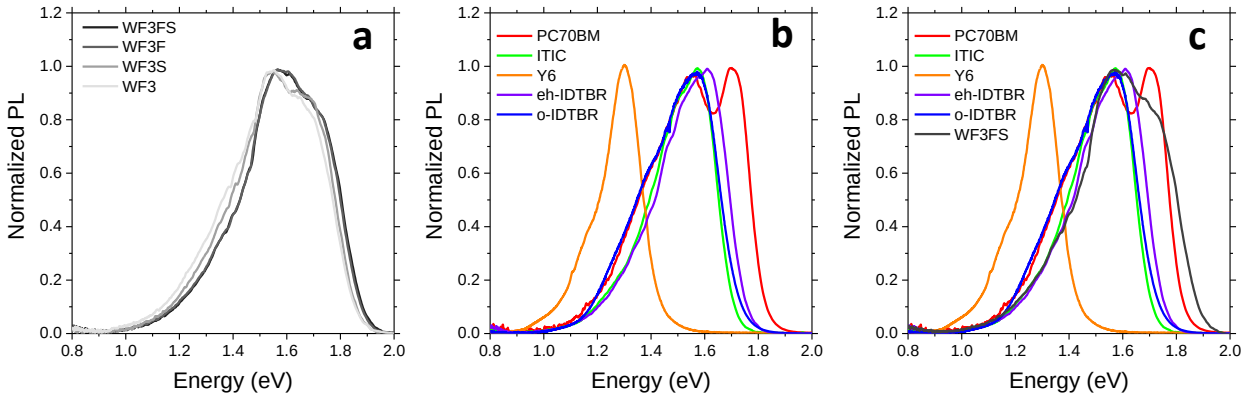

Supplementary Figure 36 | PL measurements of pristine materials used in this work. PL measurements are performend on layers on glass. **a)** Polymer donors, **b)** small molecule acceptors and **c)** small molecule acceptors together with WF3FS. We observe that WF3FS has a PL emission which extends the farthest into the higher-energy regime. This allows for a clear discrimination of donor and acceptor PL signals in blend films.

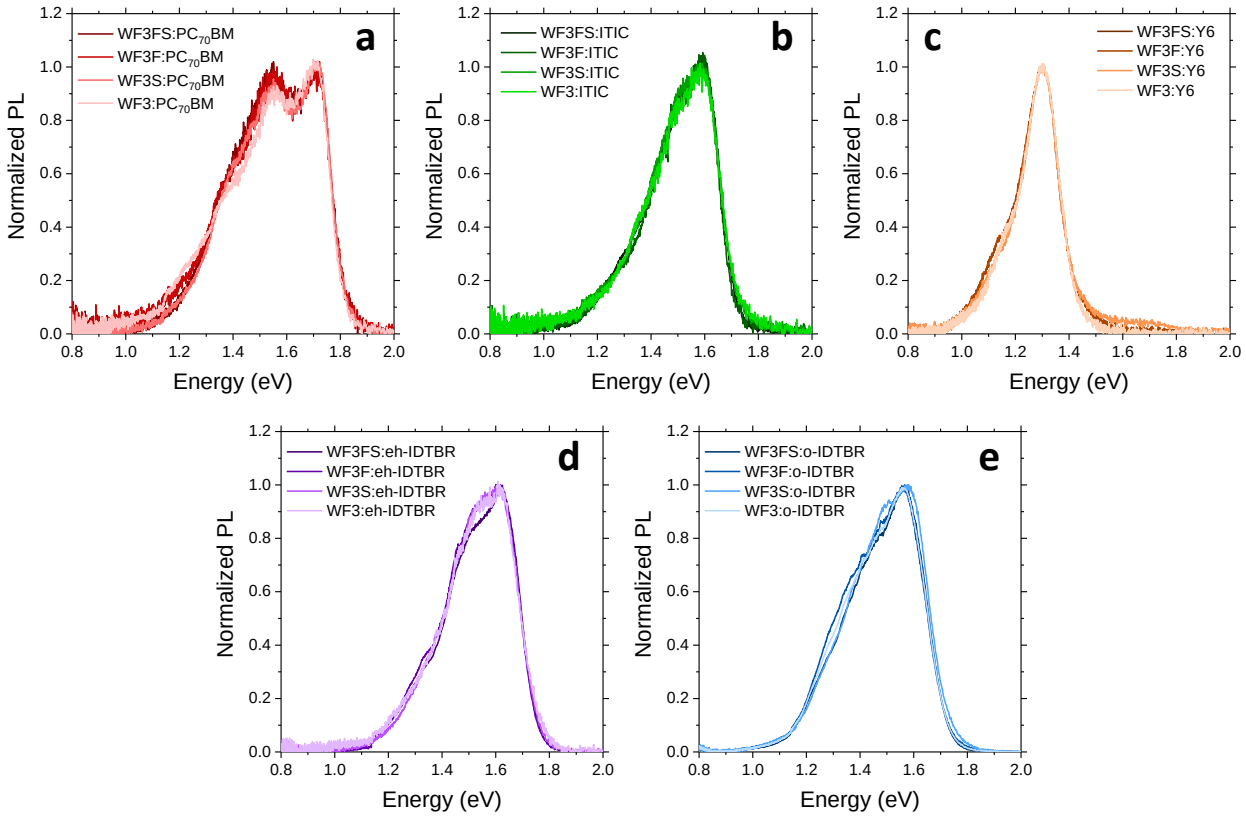

Supplementary Figure 37 | PL measurements of all solar cells investigated in this work. a) all $PC_{70}BM$ devices, **b)** all ITIC devices, **c)** all Y6 devices, **d)** all eh-IDTBR devices and **e)** all o-IDTBR devices. In all donor:acceptor bulk heterojunctions the PL signal is clearly dominated by the acceptor. We thereby infer, that the excitons on the donor are very efficiently quenched on ultra-fast time scales. For time-resolved PL measurements we deduce, that the signal is dominated by the PL of the acceptor.

Supplementary Note 4: Influence of choice of Marcus electron transfer rate constants

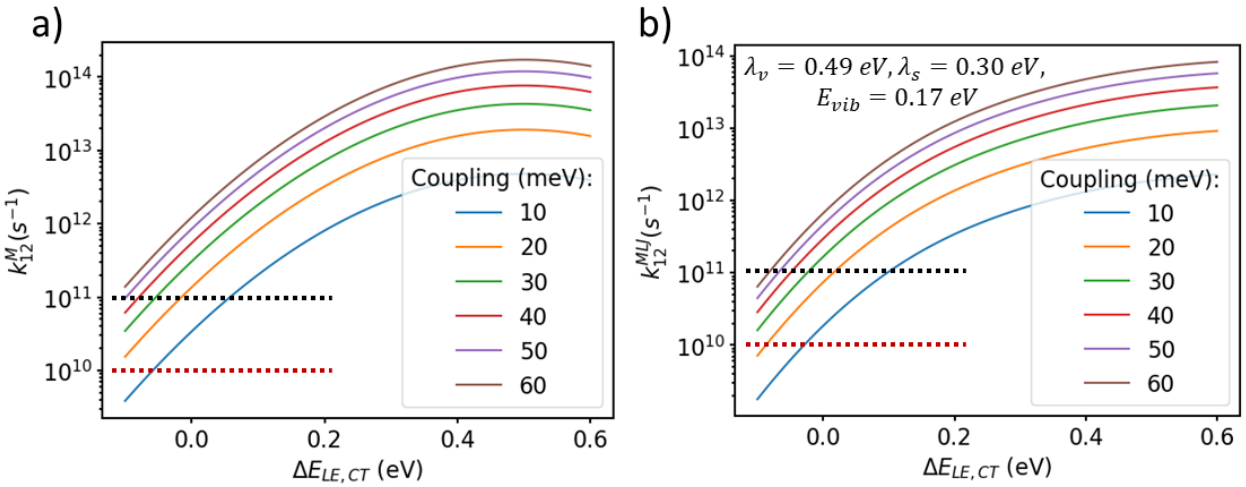

Supplementary Figure 38 | prediction of the exciton splitting rate constant. From **a)** Marcus and **b)** the Marcus-Levich-Jortner formula[9], assuming parameters as given in the inset. For further explanations, see text. The black and red dashed lines indicate the threshold below which k_{12} must explicitly be considered in the calculation of IQE and $\Delta V_{OC,nr}$, respectively.

In Supplementary Figure 38, we predict k_{12} from Marcus theory, using the classical Marcus formula in panel **a** and the the Marcus-Levich-Jortner formula in panel **b**.[7] the latter being more adapted for conjugated molecules in the condensed phase. For the calculation, we use the values $\lambda_v = 0.49eV, \lambda_s = 0.3eV$ for the internal and external reorganization energies, respectively, as given in ref[7] for a donor-acceptor dyad. We represent k_{12} for typical values of the donor-acceptor coupling strength, which has been shown to be in the tens of meV range.[9] Black and red dashed lines denote the thresholds that we have defined in the discussion of Supplementary Fig 25a and Supplementary 26f, respectively; below these thresholds, IQE and $\Delta V_{OC,nr}$, respectively, start to depend significantly on k_{12}. Supplementary Figure 38 shows that the absolute value of k_{12} can be safely ignored across nearly the whole measured range of values. Only for negative driving forces a small influence on the IQE values can be expected. We note that for high performance bulk heterojunctions, reorganization energies are expected to be much lower than those reported in ref[7] so that the k_{12} values shown in Supplementary Figure 38 are to be considered as lower limits. In conclusion, it becomes evident that as long as the reorganization energies are good enough for efficient OPV systems, knowledge of exact Marcus rates is unnecessary for the determination of IQE and $\Delta V_{OC,nr}$.

Supplementary References

1. Rau, U., Blank, B., Müller, T. C. M. & Kirchartz, T. Efficiency Potential of Photovoltaic Materials and Devices Unveiled by Detailed-Balance Analysis. *Phys. Rev. Appl.* **7**, 1–9 (2017).
2. Xie, Y. *et al.* Assessing the energy offset at the electron donor/acceptor interface in organic solar cells through radiative efficiency measurements. *Energy Environ. Sci.* **12**, 3556–3566 (2019).
3. Vezie, M. S. *et al.* Impact of Marginal Exciton-Charge-Transfer State Offset on Charge Generation and Recombination in Polymer:Fullerene Solar Cells. *ACS Energy Lett.* **4**, 2096–2103 (2019).
4. Qian, D. *et al.* Design rules for minimizing voltage losses in high-efficiency organic solar cells. *Nat. Mater.* **17**, 703–709 (2018).
5. Heiber, M. C., Baumbach, C., Dyakonov, V. & Deibel, C. Encounter-limited charge-carrier recombination in phase-separated organic semiconductor blends. *Phys. Rev. Lett.* **114**, 1–5 (2015).
6. Rau, U. Reciprocity relation between photovoltaic quantum efficiency and electroluminescent emission of solar cells. *Phys. Rev. B - Condens. Matter Mater. Phys.* **76**, 1–8 (2007).
7. Melianas, A. *et al.* Nonequilibrium site distribution governs charge-transfer electroluminescence at disordered organic heterointerfaces. *Proc. Natl. Acad. Sci. U. S. A.* **116**, 23416–23425 (2019).
8. Unger, T. *et al.* The Impact of Driving Force and Temperature on the Electron Transfer in Donor-Acceptor Blend Systems. *J. Phys. Chem. C* **121**, 22739–22752 (2017).
9. Reekie, T. A. *et al.* Porphyrin Donor and Tunable Push–Pull Acceptor Conjugates—Experimental Investigation of Marcus Theory. *Chem. - A Eur. J.* **23**, 6357–6369 (2017).